Research Square

Preprints are preliminary reports that have not undergone peer review.
They should not be considered conclusive, used to inform clinical practice,
or referenced by the media as validated information.

Flame and Shock Dynamics of a Sonic Jet in Supersonic Crossflows: Quenching, Shock-Vortex Interaction, and Flame Anchoring

Ahmed Essa

ahmed.essa@uconn.edu

University of Connecticut

Research Article

Keywords: Shock waves, Supersonic flow, Compressible Flows, Reacting Flows

Posted Date: April 1st, 2026

DOI: https://doi.org/10.21203/rs.3.rs-9272693/v1

License: This work is licensed under a Creative Commons Attribution 4.0 International License.
Read Full License

Additional Declarations: The authors declare no competing interests.

Flame and Shock Dynamics of a Sonic Jet in Supersonic Crossflows: Quenching, Shock-Vortex Interaction, and Flame Anchoring

A. Essa[1] †

[1]Mechanical, Aerospace, and Manufacturing Engineering, College of Engineering, University of Connecticut, Storrs, Connecticut, USA

(Received xx; revised xx; accepted xx)

The flame and shock dynamics of a sonic hydrogen jet injected into a confined, supersonic crossflow (Mach 2.7) are investigated. A parametric study across jet-to-crossflow momentum flux ratios (J=1.5,3.0,5.87) reveals a systematic pathway to global thermoacoustic instability. At low J, the flow is stable, characterized by coherent shock trains and weak vortices. Increasing J strengthens the counter-rotating vortex pair and Kelvin-Helmholtz rollers, which begin to deform and subsequently disrupt the shock train. At the highest J, violent shock-vortex interaction breaks down global pressure separation, generating chaotic dilatation fields. This process provides the nonlinear energy source that, as shown in prior work, feeds a domain-filling global mode. The study also resolves a longstanding debate on flame quenching. In this confined configuration, expansion regions emerge inherently downstream of the shock train. Analysis of Damkohler numbers, strain fields, and HO_2 radical maps demonstrates that while flame quenching is spatially coincident with these expansions, the fundamental cause is the excessive strain and high scalar dissipation rates sustained by the intense vortical structures (CVP, KH rollers) within them. Thus, expansion regions mark susceptible zones, but vortex-driven strain executes extinction. This finding reconciles previous contradictory explanations by showing that Gamba's ramp-induced expansion fan and the intrinsic expansions observed here both create environments where vorticity-mediated strain dominates quenching. Flame anchoring evolves from a two-dimensional, wall-attached sheet at low J to a three-dimensional structure at high J, distributed by shock-enhanced sidewall mixing and vortical redistribution from a reorganized horseshoe vortex system.

Key words: Supersonic Reacting Flow

1. Introduction

The transverse jet in supersonic crossflow has been established as a canonical configuration for fundamental supersonic combustion research. As noted by Gamba *et al.* (2011), this geometry effectively encapsulates the key physical phenomena present in practical scram-

† Email address for correspondence: ahmed.essa@uconn.edu

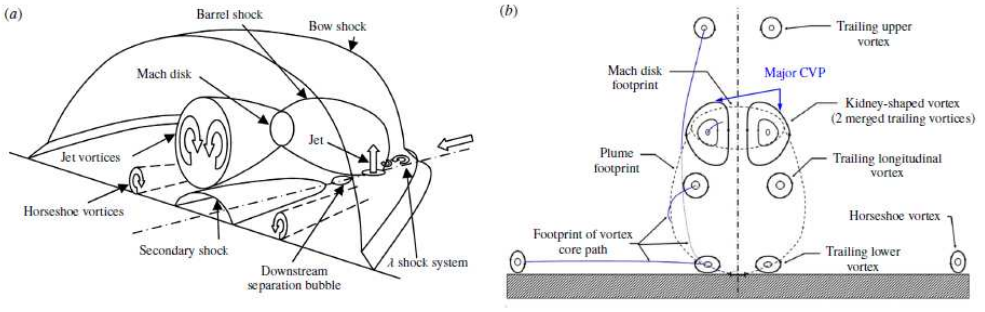


Figure 1: Schematic drawing of the flow structure of jet in a supersonic crossflow (Viti *et al.* 2009; Dickmann & Lu 2009; Sun & Hu 2018).

jet combustors—including complex shock structures, shock-boundary-layer interactions, compressible shear layers, and large-scale turbulent mixing—while remaining tractable for detailed experimental and computational study. Its utility as a model problem is demonstrated by its extensive adoption across a wide spectrum of research, from fundamental investigations of jet dynamics and mixing Huang & Yan (2013); Huang (2016); Karagozian (2010) to applied studies of ignition and flameholding in systems like the HyShot II scramjet engine Hass *et al.* (2005); Smart *et al.* (2006).

The transverse injection of a sonic jet into a high-enthalpy supersonic crossflow generates a complex system of shock waves and vortical structures, critical for mixing and combustion processes. Upstream of the injection site, viscous interactions between the crossflow and the wall result in a boundary layer, which interacts with shock waves produced by the jet obstruction. A Lip shock forms immediately upstream of the jet orifice due to the local pressure rise caused by jet expulsion, as depicted in Figure 1.

As the supersonic crossflow encounters the jet, it undergoes compression and deflection, leading to the formation of a detached Bow shock that curves around the jet plume. This shock system decelerates and turns the flow, creating adverse pressure gradients that cause boundary layer separation upstream of the jet. The separated flow culminates in a recirculation zone characterized by reverse flow and low velocities, which serves as a key mechanism for flame stabilization and holding by trapping hot gases and radicals (Gruber *et al.* 1996; Ben-Yakar & Hanson 1998).

Downstream of the jet, the wake region is dominated by a counter-rotating vortex pair (CVP), which enhances mixing between the injected fuel and the crossflow. Additional shocks, such as the barrel shock and Mach disk within the jet plume, and the collision shock at the leeward jet plume (Liang *et al.* 2018; Liu *et al.* 2019*b*, 2018), further define the flow structure. These features collectively influence ignition, stability, and combustion efficiency in supersonic combustors.

Intensive studies were conducted on the vortex structure of a transverse jet in a subsonic and a supersonic crossflow. The wake region downstream of a jet-in-crossflow is characterized by the formation of distinct tornado-like vortices, which originate from the bilateral separation of the crossflow boundary layer. These wake vortices are generated by alternating separation events on either side of the jet centerline and intensify as they propagate downstream through stretching and the continuous entrainment of boundary layer fluid. Together with other key structures—including shear layer vortices, the counter-rotating vortex pair (CVP), and horseshoe vortices—this comprehensive vortex system forms an interconnected framework that governs the complex mixing and overall flow dynamics, as initially documented (Kelso *et al.* 1996).

The assumption of symmetry in the flow field around a transverse jet has been a subject of considerable debate within the literature. While computational studies, such as the work by Muppidi & Mahesh (2006), have demonstrated that symmetric solutions are attainable under idealized numerical conditions, experimental investigations have consistently reported asymmetric structures. This discrepancy has historically been attributed to experimental artifacts; for instance, Smith & Mungal (1998) argued that manufacturing defects in the injector geometry were the primary cause. Through meticulous refinement of their setup, they were able to achieve symmetric flow at momentum flux ratios ($\sqrt{J}$) below 10, but observed inherent asymmetries at higher ratios, suggesting a transition to instability-dominated dynamics.

Subsequent research has provided a more nuanced understanding, indicating that asymmetry is often an intrinsic feature of the flow physics. The experimental work of Gevorkyan *et al.* (2016) demonstrated that pronounced asymmetry correlates with increasing velocity ratio and is stabilized by lower density ratios for a constant J. They identified that the asymmetry originates from hydrodynamic instabilities, specifically an asymmetric vortex roll-up in the shear layers due to differential straining and the nonlinear interaction of a tertiary vortical structure with the primary counter-rotating vortex pair (CVP). This body of work reconciles the computational-experimental discrepancy by confirming that while symmetry can be achieved under carefully controlled conditions—both numerically and experimentally—beyond a certain threshold of velocity or momentum flux ratio, inherent flow instabilities dominate and promote asymmetric structures.

The injection of an underexpanded sonic jet into a supersonic crossflow generates a complex shock structure, characterized by a barrel shock (BS2) terminated by a Mach disk (Fig. 1). This structure induces significant flow features: a downstream recirculation zone forms on the leeward side, followed by a secondary shock, while the windward side is enveloped by horseshoe vortices. These vortices are critical, as they efficiently transport fuel into the broader, OH-rich regions of the flow (Zhao *et al.* 2017). The OH mass fraction concentration was used by previous studies as indication for the flames in the Hydrogen-air systems (Gamba *et al.* 2011; Gamba & Mungal 2015; Candler *et al.* 2017; Laurence *et al.* 2013; Sharma *et al.* 2024*a*,*b*; Attili *et al.* 2014; Rasheed & Mishra 2023; Liu *et al.* 2019*a*).

Wang *et al.* (2025) constructed an experimental setup to investigate the effect of a streamwise vortex on the shock train across different flow Mach numbers. The experiment was conducted for three different vortex intensities. They found that an increase in streamwise vortex intensity dampened the shock train's self-excited oscillations while simultaneously intensifying pressure fluctuations caused by motion of the shock train leading edge. The streamwise vortices interfered with and bifurcated the oblique shock wave. This deformation became more severe with increasing vortex intensity and downstream development. At M = 2.01, moderate and strong vortices caused the Mach stem at the shock train leading edge (STLE) to bend upstream. Conversely, at the higher Mach number of M = 2.81, vortices of similar strength caused the top- or bottom-wall shock waves within the STLE to bend and bifurcate into multiple shock waves.

The motion of a shock train in response to downstream high-frequency pressure excitations is driven by disturbances traveling upstream through the subsonic boundary layer, forcing the shock train into periodic oscillation. Unlike a steady shock train, which adjusts its position to match a fixed back pressure, an unsteady shock train moves continuously to modulate the relative Mach number ahead of it, thereby matching the dynamically varying back pressure (Xiong *et al.* 2018).

Nie *et al.* (2024) discussed the influence of the nitrogen concentration on quenching the hydrogen-air system's flames in microchannels. By adding an inert, e.g. nitrogen, more

amount of the energy released by the combustion because of their high heat capacity. Thus, the flammability limits will become narrower as the adiabatic flame temperature decrease should dilutes the flames thermally.

The LES study by Zhao *et al.* (2017) of a hydrogen jet in a supersonic crossflow reveals significant geometric dependencies in flame stabilization and combustion modes, leading to substantive disagreements with the foundational work of Gamba *et al.* (2011, 2012). While Zhao et al. confirm that the shock train from an inlet ramp enhances near-wall combustion—promoting premixed and partially premixed flames in recirculation zones—their findings challenge Gamba's core interpretations of flame dynamics. Crucially, they attribute local extinction downstream not to Gamba's proposed mechanism of expansion fan interference but rather to high scalar dissipation rates from large velocity gradients, a phenomenon observed even in the absence of a ramp. Furthermore, discrepancies in observed jet penetration and the intensified, shock-induced combustion modes highlight the profound influence of specific inlet configurations. These results suggest that Gamba's conclusions, particularly regarding expansion fan effects, may be geometry-specific and not fully account for the universal role of scalar dissipation in flame quenching. Thus, the study by Zhao *et al.* (2017) provides a critical alternative framework for understanding extinction and stabilization, emphasizing shock-enhanced mixing and dissipation rates while underscoring that inlet geometry dictates the dominant combustion physics in supersonic flows.

This paper is structured as follows. Section 2 presents the governing equations and the hydrogen–air reaction mechanism employed. Section 3 describes the computational model, including the domain configuration, boundary conditions, and the three injection cases studied. Section 4 examines the global shock–vortex interaction, revealing how increasing momentum flux ratio transforms the flow from a shock-dominated, stable regime to a vortex-driven globally unstable one. Section 5 analyzes flame anchoring, topology, and quenching, demonstrating through Damkohler, strain, and radical diagnostics that local extinction is executed by vortex-amplified strain, not expansion fans, thereby reconciling prior contradictory explanations. Finally, Section 6 synthesizes these findings into a unified model of flame–shock–vortex coupling in confined supersonic flows and discusses implications for combustor design.

2. Governing Equations

A predominant methodology in the study of transverse jets in supersonic crossflow involves the use of hydrogen-based chemical systems to model the reacting flow field, as extensively employed by studies such as Gamba *et al.* (2011); Gamba & Mungal (2015); Zhao *et al.* (2017); Fu *et al.* (2019); Rasheed & Mishra (2023). This approach provides significant advantages by substantially reducing the complexity of chemical kinetics while still capturing the essential physics of supersonic combustion, such as intense heat release and compressibility effects. The resulting simplified reaction mechanisms render high-fidelity computational simulations—including large-eddy and direct numerical simulations—more tractable and facilitate a clearer interpretation of the coupled fluid-chemistry interactions in experimental work.

However, this modeling strategy inherently abstracts away complexities inherent to practical hydrocarbon fuels, such as pyrolysis, soot formation, and longer ignition delay times. Despite this limitation, the hydrogen-modeling paradigm has proven highly effective for isolating fundamental combustion phenomena, including auto-ignition, flame stabilization, and blow-off mechanisms, thereby providing a foundational understanding that can inform the analysis of more complex multi-component reactive systems.

The governing equations for compressible reactive flow—namely the Navier-Stokes

equations for mass, momentum, energy, and species transport, along with the equation of state for a multi-species, thermally perfect gas—are solved using the numerical framework described in detail in Essa (2026). The simulations employ the Athena-RFX++ solver (Stone *et al.* 2024, 2020, 2008), which features dynamic patch-based adaptive mesh refinement (AMR) and a fully unsplit corner transport upwind (CTU) scheme coupled with an HLLC Riemann solver (Toro 2013). This methodology ensures high-fidelity capture of multi-dimensional wave propagation, shock interactions, and turbulent combustion phenomena. The reader is referred to Essa (2026) for a complete presentation of the governing equations, thermodynamic closure, and numerical implementation.

The Athena-RFX/Athena-RFX++ solvers are well-established in the combustion community, with their numerical framework and convergence properties rigorously validated across a wide range of turbulent combustion problems (Ezra & Kozak 2023; Poludnenko *et al.* 2011, 2019; Jozefik *et al.* 2024). This body of work confirms the solver's suitability for high-fidelity simulations, providing confidence in its numerical stability and predictive accuracy for the present study.

To characterize the combustion regime, the Damkohler number was evaluated. This dimensionless number represents the ratio of a turbulent mixing time scale to a chemical reaction time scale:

$$Da = \frac{\tau_t}{\tau_c} \tag{2.1}$$

where τ_t is the turbulent mixing time and τ_c is the chemical time.

The structure of the turbulent flow field was analyzed using the Q-criterion. This method defines a vortex core as a connected region with a positive second invariant of the velocity gradient tensor, which is expressed as:

$$Q = \frac{1}{2}\left(||\Omega||^2 - ||S||^2\right) >> 0 \tag{2.2}$$

Here, $S = \frac{1}{2}(\nabla\mathbf{u} + \nabla\mathbf{u}^T)$ is the symmetric strain rate tensor and $\Omega = \frac{1}{2}(\nabla\mathbf{u} - \nabla\mathbf{u}^T)$ is the anti-symmetric vorticity tensor. A positive Q value signifies a region where rotational forces dominate over straining forces, highlighting coherent vortical structures.

The Takeno Flame Index (FI) was adopted to delineate the local combustion regime within the flame. This approach was chosen over alternative methods (Zhang *et al.* 2019; Liu *et al.* 2019*a*; Potturi & Edwards 2015; Li *et al.* 2024) for its physicochemical interpretability and its ability to provide a clear, unambiguous distinction between premixed and non-premixed reaction zones.

The FI is defined based on the relative orientation of the fuel and oxidizer mass fraction gradients:

$$\mathrm{FI} = \frac{\nabla Y_\mathrm{F} \cdot \nabla Y_\mathrm{O}}{|\nabla Y_\mathrm{F}|\,|\nabla Y_\mathrm{O}|} \tag{2.3}$$

where Y_F and Y_O are the mass fractions of the fuel and oxidizer, respectively. A positive FI ($\nabla Y_\mathrm{F} \cdot \nabla Y_\mathrm{O} > 0$) indicates fuel and oxidizer diffusing in the same direction, characteristic of a premixed flame. Conversely, a negative FI ($\nabla Y_\mathrm{F} \cdot \nabla Y_\mathrm{O} < 0$) indicates them diffusing towards each other from opposite sides of the reaction zone, characteristic of a non-premixed flame.

To ensure numerical robustness and prevent division by infinitesimally small values in regions of negligible scalar gradients, a threshold was implemented. The denominator in Eq. (2.3) was only evaluated if the product $|\nabla Y_\mathrm{F}|\,|\nabla Y_\mathrm{O}|$ exceeded a minimum value ϵ, determined based on the maximum gradients present in the domain, where this product was below ϵ were considered inert and assigned an FI of zero.

3. Computational Model

The computational configuration consists of a square channel with a height of 4.5 cm, replicating experimental setups for transverse jet in supersonic crossflow studies. A complete description of the domain design, boundary treatments, grid resolution strategy, and validation is provided in Essa (2026); only essential parameters are summarized here.

The domain extends from $x = 0$ to 40 cm, with an injector of radius 1.6 mm positioned at $x = 8.4$ cm. No-slip adiabatic conditions are applied on all walls following an initial short slip-wall region at the inlet to prevent spurious numerical reflections. Dynamic patch-based adaptive mesh refinement (AMR) yields an effective uniform grid spacing of approximately 87 μm after the initial transient, resulting in > 550 cells across the channel height and 25-62 cells within the incoming boundary layer, with a first cell at $y^+ \approx 8 - 10$. This resolution, classified as quasi-direct numerical simulation (QDNS), follows the criteria established in Essa (2026) and is sufficient to capture the large-scale, energy-containing structures governing global instabilities in high-speed flows (Poludnenko & Oran 2010). Grid convergence and validation of the present setup against experimental data are documented in Essa (2026).

The supersonic crossflow inlet conditions are set to a Mach number of 2.7 with a static pressure of 0.75 bar and a static temperature of 1400 K. A sonic hydrogen jet at 300 K is injected normal to this crossflow. Three injection cases are examined, defined by jet-to-crossflow momentum flux ratios (J) of 1.5, 3.0, and 5.87. The required jet static pressures to achieve these J values, calculated via Eq. (3.1), are 7.67, 15.33, and 30.0 bar, respectively.

$$J = \frac{(p\gamma M^2)_j}{(p\gamma M^2)_\infty} \tag{3.1}$$

In Eq. (3.1), the subscripts j and ∞ refer to jet and crossflow conditions, M is Mach number, and γ is the specific heat ratio.

4. Global Structure of Reacting Transverse Jet

4.1. *Shock Structure*

The shock topology arising from a transverse jet in a supersonic crossflow (JISCF) is a complex system of interacting waves and vortical structures, central to mixing and combustion processes in scramjet engines. The flowfield, initiated upstream of the injection port, is characterized by the interaction of the jet, which acts as a bluff body, with the oncoming crossflow.

Ahead of the jet, the imposition of a no-slip boundary condition at the bleed point (x = 2 cm) ensures a developed boundary layer, as depicted in Figure 2. This decelerated flow leads to the formation of leading lip shocks (LS). Subsequent boundary-layer separation induces a separation shock (SS) and creates an upstream separation/recirculation zone (USR), which facilitates the genesis of a horseshoe vortex (HSV) wrapping around the jet periphery.

The jet plume itself obstructs the supersonic freestream, generating a strong, curved bow shock (BS1) that decelerates the flow prior to its diversion around the jet. The interaction of this bow shock with the upper-wall boundary layer causes further separation, creating distinct separation regions (SR) (Figures 3b-d and 4b-d). The diverted flow around the jet exhibits shear instability, giving rise to Kelvin-Helmholtz (KH) waves due to the velocity differential between the fuel jet and the crossflow. This shear is also the primary driver for the formation of the dominant counter-rotating vortex pair (CVP), which is an essential mechanism for large-scale mixing downstream the injection.

Immediately downstream of the jet, the flow is characterized by separation bubbles, a reattachment zone, and wake structures (WS) that contribute to the sustenance of the CVP.

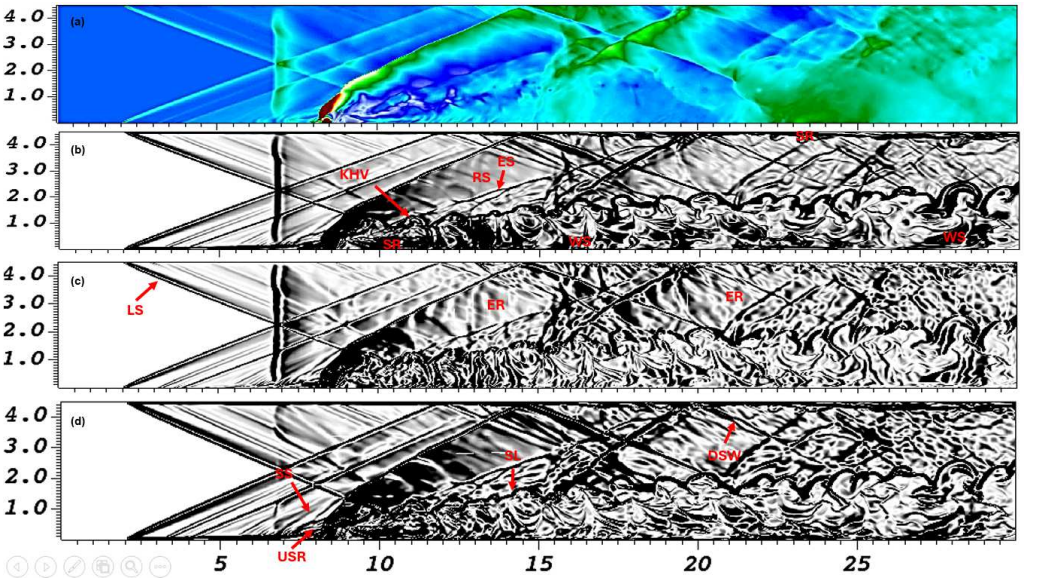


Figure 2: The shock structure in the streamwise direction for J=1.5: (a) pressure contour, (b) density gradient magnitude, (c) the density gradient in streamwise direction, and (d) the density gradient in the wall-normal direction.

The jet is enveloped by a barrel shock, terminated by a Mach disk, which collectively form an envelope shock (ES). The entire flowfield is further complicated by shock-shear layer and shock-boundary layer interactions, which disrupt the shock train, giving rise to compression waves (CW), expansion regions (ER), and deformed shockwaves (DSW).

A critical feature of this interaction is the shock-vortex interplay, which can significantly alter the shock topology. In extreme instances, this interaction leads to high shock angles, resulting in the formation of a triple point (TP) and a Mach stem, behind which the flow undergoes intense compression due to the near-normal shock condition. A schematic illustrating the profound effect of this shock-vortex interaction is presented in Figure 5.

The spatial and temporal evolution of the bow shock incidence on the upper wall exhibits a strong dependence on the momentum flux ratio (J), demonstrating distinct stabilization characteristics across the tested flow conditions. For lower momentum flux ratios (J=1.5 and 3), the bow shock incidence forms at progressively upstream locations (x=14.5 cm and 12.9 cm, respectively), indicating enhanced shock stabilization with increasing J. However, the higher momentum flux ratio condition (J=5.87) reveals more complex dynamics, where the bow shock incidence anchors at x=11.3 cm at t=1.5 ms but subsequently exhibits temporal variations due to downstream pressure accumulation. This unsteady behavior manifests through the development of a propagating normal shockwave, which modulates the local flow topology and induces oscillations in the susceptible Mach stem position—bow shock incidence location. The observed trends suggest that while higher momentum flux ratios generally promote upstream shock migration, the transition to choked flow introduces competing mechanisms between pressure accumulation effects and shock stabilization processes, leading to time-dependent variations in the shock system configuration.

The height of the upstream separation zone (USR) exhibits a clear, positive correlation with the momentum flux ratio, J. The separation zone thickness prior the injection point increases from 2.5 mm to 5 mm as J rises from 1.5 to 5.87, with an intermediate value of 3 mm at $J = 3$, as shown in figures 2b, 3b, and 4b. This systematic growth indicates a significant

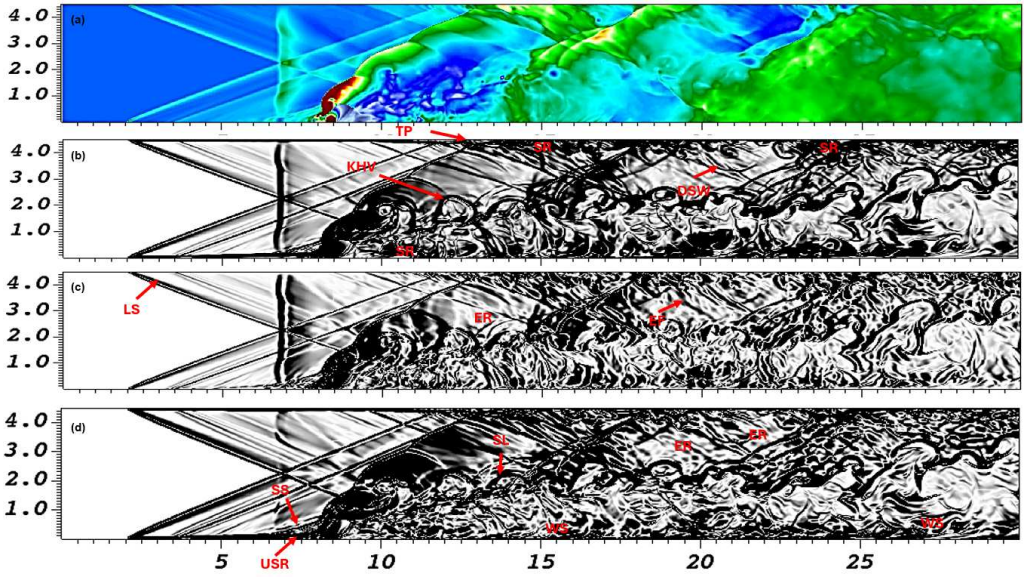


Figure 3: The shock structure in the streamwise direction for J=3: (a) pressure contour, (b) density gradient magnitude, (c) the density gradient in streamwise direction, and (d) the density gradient in the wall-normal direction.

enhancement of flow reversal and recirculation strength upstream of the jet injection site. The trend is directly linked to the development of larger-scale vortical structures, particularly the horseshoe vortex, which becomes more pronounced under the intensified jet–crossflow interaction at higher J.

The expansion of the upstream separation zone signifies a fundamental shift in the shock–boundary layer dynamics. The increased jet momentum flux induces greater flow deflection, strengthening the adverse pressure gradient ahead of the jet and resulting in a more extensive region of separated flow. The strong correlation between the separation zone height and the scale of the vortical structures provides critical insight into the mechanisms governing mixing and flame stabilization in this system. Specifically, the larger recirculation zones and vortices generated at higher J values are expected to profoundly enhance scalar transport, fuel-air mixing, and combustion dynamics in the near-wall region. Figure 5 schematically illustrates the complex interplay of compressible and vortical structures generated by a transverse jet in a supersonic crossflow. The flow field is characterized by a hierarchy of interacting features, each resulting from the fundamental obstruction and momentum imbalance introduced by the jet. Immediately upstream of the injection point, the supersonic crossflow encounters the jet as a bluff body, generating a detached bow shock. This shock decelerates and deflects the incoming flow, inducing a strong adverse pressure gradient that causes boundary layer separation. This separation culminates in a recirculation zone upstream of the jet, as mentioned earlier.

The interface between the injected sonic jet and the supersonic crossflow is a site of intense shear, leading to the development of a shear layer. This layer is susceptible to Kelvin-Helmholtz (K-H) instabilities, visible as large-scale rolling structures. These coherent vortices significantly distort the contact surface and act as secondary obstacles to the oncoming flow. Consequently, they force the formation of additional oblique shock waves to turn the flow. Depending on the incident shock angle, a transient Mach stem can form (Figure 5), with

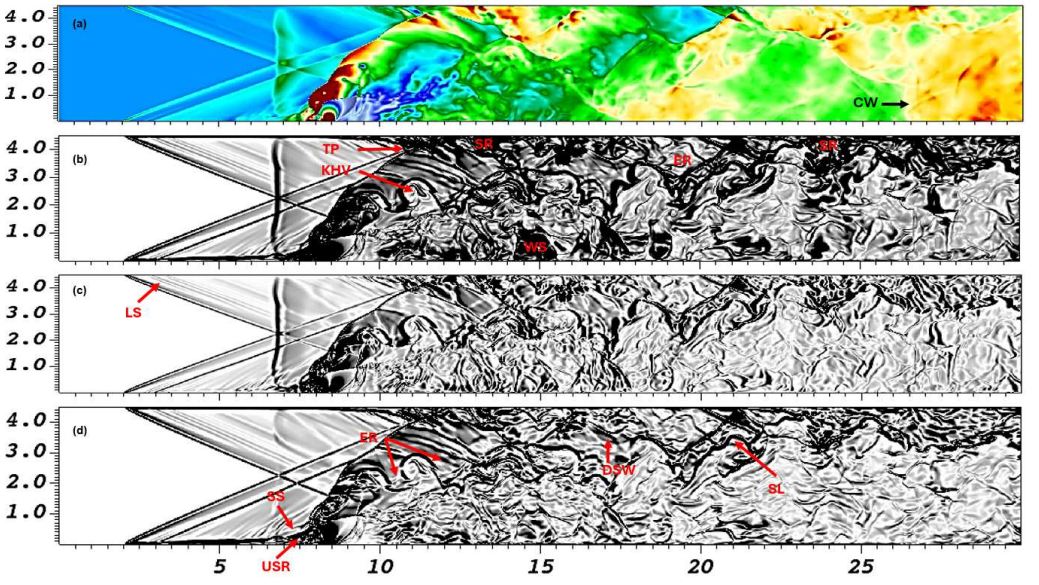


Figure 4: The shock structure in the streamwise direction for J=5.87: (a) pressure contour, (b) density gradient magnitude, (c) the density gradient in streamwise direction, and (d) the density gradient in the wall-normal direction.

its persistence governed by the local flow dynamics and the structural state of the counter-rotating vortex pair.

Separation zones also critically influence shock formation. The establishment of separation bubbles—whether from shock-boundary layer interaction or classical adverse pressure gradients—forces the development of new shockwaves. This process can lead to complex X-shaped shock structures and Mach stems due to the intersection between the reflected shockwaves of the shock train and the new developed shockwaves (Wang *et al.* 2024).

Downstream of the jet, the counter-rotating vortex pair dominates the wake structure. The interaction of shockwaves with these strong vortical regions leads to pronounced shock deformation and bifurcation, as the rotational core of the vortex locally alters the wave angle and stability. The shock train is notably disrupted by the CVP. The shock-vortex interaction leads to visible shock deformation and bifurcation, as clearly indicated in Figures 2, 3, and 4.

Conversely, distinct expansion fans are observed on the upper wall, downstream of separation zones. Here, compression waves suppress the separation layer thickness, creating a region where the supersonic flow can expand. These expansion zones were consistently noted in all cases studied: between x = 18–22 cm for J = 1.5 and J = 3.0 (Figures 2c and 3d), and between x = 19–20 cm for J = 5.87 (Figure 4b). The reduction of this expansion zone at the higher momentum flux ratio (J = 5.87) is directly related to the stronger compression wave evident at the downstream in Figure 4a. The presence of these fans, alongside the complex shock train, highlights the highly three-dimensional and unsteady nature of the interaction, where regions of compression and expansion exist in close proximity, driven by the evolving vortical structures.

The flow field for the lowest momentum flux ratio case exhibited a markedly more stationary shock train structure compared to the higher-J cases. This enhanced stability is attributed to the reduced scale of the Kelvin-Helmholtz (KH) waves developing in the shear layer. Their diminished size resulted in a smoother windward face of the counter-rotating vortex

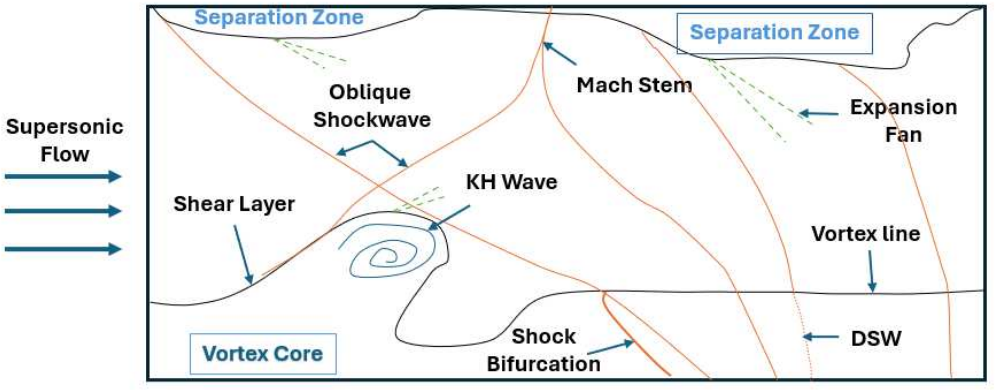


Figure 5: Schematic two-dimensional diagram of shock-vortex interaction.

pair (CVP), which presented a less perturbed effective aerodynamic surface to the oncoming crossflow.

Consequently, the flow required fewer compensatory shockwaves to negotiate around the CVP structure. This was further facilitated by a relatively stable boundary layer on the upper wall. The combined effect of these factors—reduced KH instability, a smoother CVP, and a stable boundary layer—resulted in a less complex wave structure, yielding clearer schlieren images that cleanly captured the envelope shock topology. This underscores the results of Sun & Hu (2018), confirming that the clarity of the envelope shock diminishes with increasing J due to the enhanced unsteadiness and interfacial complexity introduced by the stronger jet.

The near-wall downstream separation zone (DSZ) is crucial for understanding the shocks that are generated and the behavior of vortices—both their termination and formation—on the lower wall. In Figure 6, the pressure distribution (top half) shows a low-pressure region downstream of the injector. The schlieren images (lower half of Figure 6) reveal large density variations around the separation zone. This separation zone arises in the flow field due to the low-pressure zone that forms behind the high-pressure jet, which creates a recirculation region on the leeward side of the jet. The density variations provide a clear visual means of identifying the separation zone.

It was observed that the size of the downstream separation zone increases with an increase in J. However, in extreme cases, the DSZ can also expand in the spanwise direction. This occurs due to the downstream compression region (shown in red in Figure 6c) and the reduced speed of the crossflow after it passes through a stronger bow shock upstream of the injector which allows the collision shock to be wider.

The downstream separation zone acts as a blockage to the crossflow, which wraps around the jet plume at supersonic speed. This leads to the formation of a shock at the upstream edge of the separation zone. This shock is referred to as a collision shock because it results from the crossflow colliding with the initial separation bubbles of the separation zone. At the peak of the separation zone, an expansion fan is formed, consistent with the earlier discussion regarding Figure 5. The expanded flow then decelerates in order to reattach to the wall at the reattachment valley, forming another shockwave in the process, known as the reattachment shock. This region is characterized by wake vortices that feed into the counter-rotating vortex pair. The deflection angle is nearly constant for different momentum flux ratio (Sun & Hu 2018; Liu *et al.* 2018)

However, the question of the deflection angle's dependency changes fundamentally with geometric confinement. Xiong *et al.* (2022) demonstrated that the deflection angle was higher

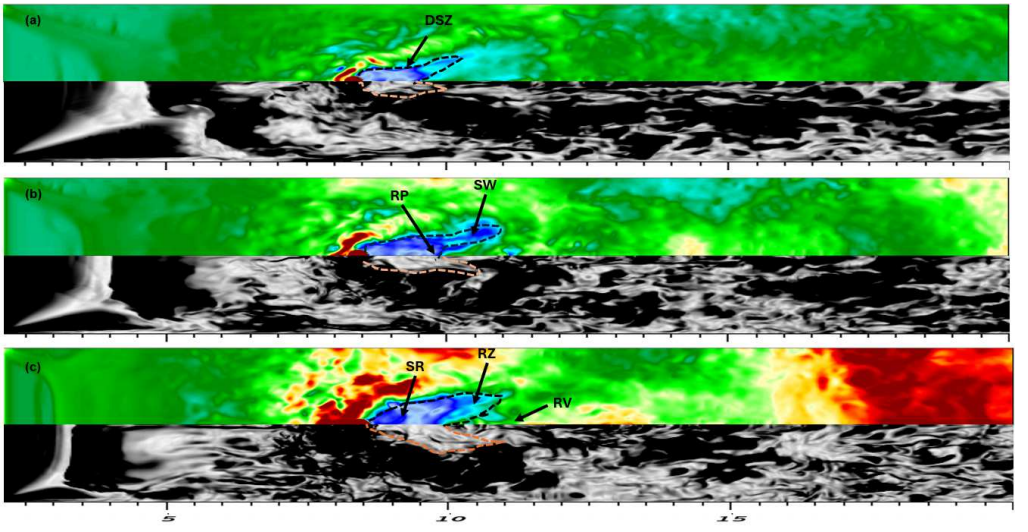


Figure 6: The instantaneous static pressure (upper half) and schlieren (bottom half) of y≈44 microns plane: (a) J=1.5, (b) J=3.0, and (c) J=5.87.

in a pipe flow compared to a rectangular channel, indicating that lateral confinement and the lower-wall significantly alter the shock-boundary layer interaction dynamics. Therefore, the independence of the deflection angle from J may be a specific feature of flat-plate or weakly confined flows, and not a universal rule for all transverse jet configurations.

The schlieren images of different slices location in the lateral plane (XY-plane) were presented in Figure 7 for the three cases. There are a clear difference between them in the shock structure. For J=1.5 and x=9 cm, the Mach disk and the barrel shock (BS2) were clearly captured there, while for the higher J cases, the barrel shock was not terminated by the Mach disk. For the highest J, KH vortex was clearly captured on the top of the barrel shock. On the sides of the lower wall, the smallest J experienced a relatively small boundary layer thickness compared to the other two cases. For J=5.87, the boundary layer was much more announced on the side and the lower walls, as an evidence for the stronger vortical structures generated by the upstream separation zone.

Another slice was taken to cut the V-shaped downstream separation zone at x=10 cm. For J=1.5, the envelop shock was clearly captured while KH vortices were almost a part of the CVP. However, the lip shock was noticed to exist on the upper edge of the CVP. For the intermediate J, KH vortices were almost separated from the CVP, and a wing-shaped shock was found closer to the lower wall. While the highest J experienced the presence of the separation shock almost combining with the Bow shock. Also, the upper and side walls experienced bigger separations, introducing more shocks to the flow. The trailing lower vortex was obviously seen close to the lower wall for J=3 and 5.87.

As we go downstream, separation regions started to be noticed in the three cases. The size of the separation regions increases by increasing J. The shockwave train footprint in the lateral slices is still visible in the downstream of J=1.5 and 3. However, it is clearer in J=1.5, but for the J=5.87, the CVP was found to be in a direct interactions with the separation zones generated on the upper and side walls damping any shockwaves there. Moreover, the wakes were more actively feeding the counter-rotating vortex pair, as more separation bubbles were generated on the lower wall as will be discussed in the next subsections.

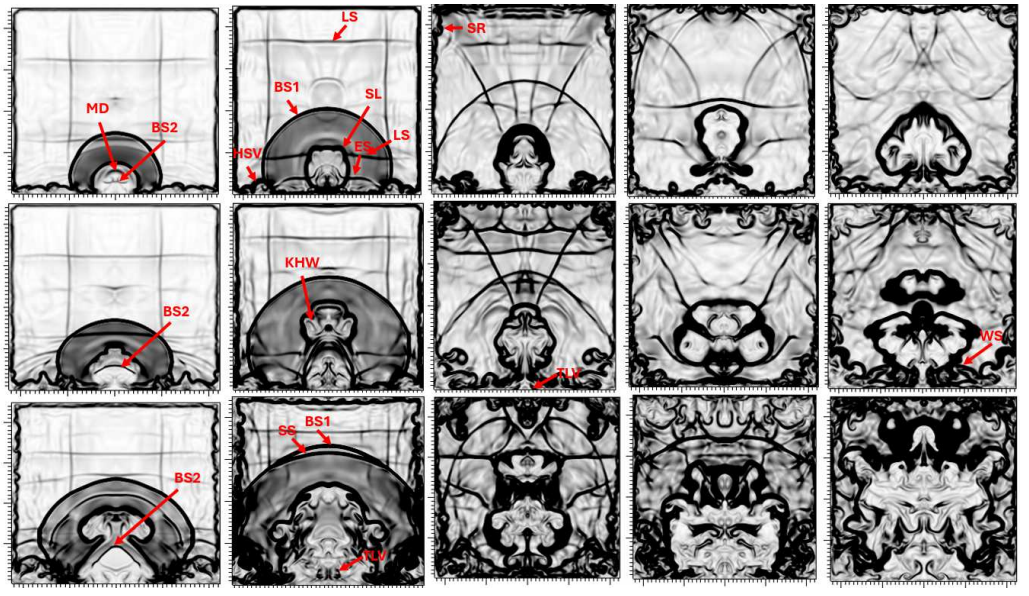


Figure 7: Schlieren images for different momentum flux ratio (J=1.5, 3.0, and 5.87) and slices of the lateral direction (YZ) plane downstream the injector (x=9, 10, 15, 20, and 25 cm): J increases from the top to the bottom, and x increases from left to right.

4.2. *Vortex Structure*

The upstream and downstream separation zones were one of the essential sources of the vortex generation in the current configuration. Sun & Hu (2018) studied the formation and the termination of the trailing lower vortex pair in the downstream recirculation zone. On the other hand, the upstream recirculation zone generates one of the characteristic vortices of the jet in crossflow in general which is the horseshoe vortex. In Figure 9, it is shown that there are three vortices generated by this region. The one sheltering the jet is the hanging vortex, while another two vortices were generated at the early stages of the upstream recirculation zone (Miller *et al.* 2018). In the confined configuration, these vortices were lifted up at the downstream enforcing the boundary layer separations on the side walls.

Figure 8, depicting the streamwise vorticity, illustrates the evolution of the vortical structure with both momentum flux ratio (J) and streamwise distance. At the lowest J, the vortex strength decays rapidly downstream. Despite this decay, the coherence of the counter-rotating vortex pair (CVP) remains intact, undisturbed by Kelvin-Helmholtz (KH) instabilities. A trailing lower vortex pair is evident at x=10 cm but dissipates shortly thereafter, indicating its limited spatial survival. They are usually generated by the strong spanwise pressure gradient (Sun & Hu 2018) and rotating in the opposite direction.

For the moderate momentum flux ratio (J=3.0), two distinct vortices (S1 and S2) are present adjacent to the barrel shock at x=9 cm. These structures merge by x=10 cm, forming the canonical CVP. Progressing downstream, the vortex cores converge, a mechanism consistent with the observations of Xiao *et al.* (2024). Large-scale shear-layer roll-ups become pronounced by x=10 cm. By x=20 cm, the CVP core exhibits high streamwise vorticity, accompanied by near-wall vortical structures generated by the complex horseshoe vortex system.

At the highest momentum flux ratio (J=5.87), the flow exhibits more intense dynamics. The S1 vortex is prominently observed in isolation flanking the barrel shock, in agreement to Xiao *et al.* (2024). While the vortex merging process is similar to the moderate J case, the resulting

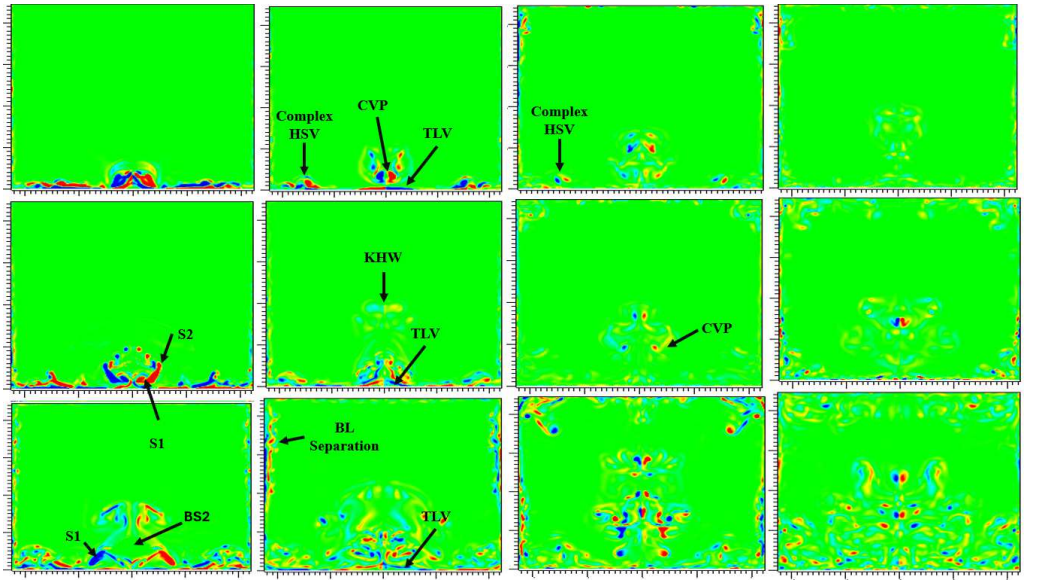


Figure 8: Streamwise vorticity for different momentum flux ratio (J=1.5, 3.0, and 5.87) and slices in the lateral direction (YZ) plane downstream the injector (x= 9, 10, 15, and 20 cm): J increases from the top to the bottom, and x increases from left to right.

Table 1: Peak vorticity within the counter-rotating vortex pair (CVP) core for each momentum flux ratio (J) at t=1.5 ms. The normalized vorticity is defined as $\omega^* = \omega L/U$, where L is the injector's diameter and U is the crossflow velocity.

J	Peak CVP Vorticity ($\times 10^6 s^{-1}$)	Normalized Vorticity	%Increase from J=1.5	Streamwise Vorticity Min ($\times 10^6 s^{-1}$)	Max ($\times 10^6 s^{-1}$)
1.5	5.425	8.9	—	-4.41	5.094
3.0	6.408	10.517	+18.17%	-5.59	5.441
5.87	7.764	12.74	+43.1%	-6.18	5.243

flow field is characterized by significantly stronger vorticity regimes downstream, indicating a more robust and powerful CVP. Furthermore, pronounced boundary layer separations on the upper and side walls generate strong, coherent streamwise vortical regions, highlighting the intensified global interaction at this condition.

Elevated momentum flux ratios enhance jet penetration, thereby increasing the effective blockage to the crossflow. This intensified jet-crossflow interaction has a dual effect: it suppresses the dominant counter-rotating vortex pair (CVP) while simultaneously generating smaller, secondary trailing vortex pairs above and below it. The coalescence of these vortex systems significantly augments the overall vorticity strength in the flow. The lower trailing vortex pair rotates in opposition to the primary CVP, whereas the upper pair exhibits either co- or counter-rotating alignment. This complex, multi-layered vortical field, particularly prominent at J=5.87, directly manifests in the highly intricate and disturbed shock patterns observed in Fig. 7. It occurred in a significantly lower pressure ratios than the unconfined flows compared to those which reported by Xiao *et al.* (2024).

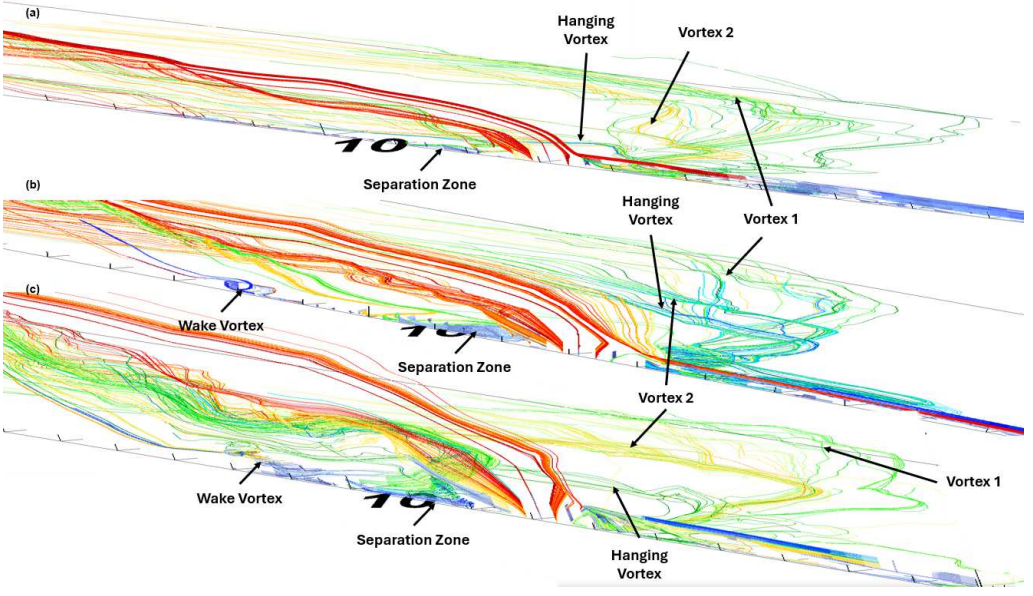


Figure 9: The generated streamlines by the upstream and downstream recirculation zones: (a) J=1.5, (b) J=3.0, and (c) J=5.87.

To quantify the evolution of the dominant vortical structures with increasing momentum flux ratio, a control volume ($x = 9.5-30$, $y = 0.3-3.5$, $z = 0-0.5$) was defined to encompass the primary counter-rotating vortex pair. The integrated streamwise vorticity within this region revealed a systematic increase in magnitude with J (Table 1), indicating enhanced overall rotational energy. More significantly, analysis of the vorticity distribution showed that the secondary, anticlockwise trailing vortex pair intensifies disproportionately relative to the primary clockwise CVP as J increases. This represents a fundamental redistribution of vortical energy within the flow, where the trailing vortex system grows to rival the primary CVP in rotational intensity. Table 1 presents instantaneous streamwise-vorticity integrals within the CVP control volume at a representative time step during the quasi-steady choking phase (J=5.87) and unchoked phases (J=1.5, 3.0). This snapshot illustrates that such vorticity redistribution occurs periodically.

It is important to note that time-averaged statistics would differ due to the distinct temporal evolution of vorticity for each J: while vorticity magnitude grows monotonically with time for J=5.87 during choking, it fluctuates about a mean for J=1.5 and 3.0. Therefore, Table 1 does not represent a steady balance, but rather one instantaneous realization of the ongoing mode competition between the CVP core and the trailing vortex pair.

Notably, this complex vortical breakdown occurs at significantly lower pressure ratios ($\approx$ 40) than those reported for unconfined flows (PR = 50) by Xiao *et al.* (2024). This earlier transition is attributed to the confinement effects of the channel, which amplify the jet-crossflow interaction and accelerate the instability dynamics.

The evolution of the vortical field with increasing momentum flux ratio is characterized by a significant intensification and increased dominance of the coherent structures. As quantified in Table 1, the peak vorticity within the core of the counter-rotating vortex pair increased systematically by 43.1% from J=1.5 to J=5.87. This quantitative strengthening is directly visualized by the Q-criterion iso-surfaces in Figure 10. While a CVP is present in all cases, its structural intensity at the J=1.5 condition is comparatively weak, falling below the visualization cutoff shortly downstream of the injection site. In contrast, the CVP for

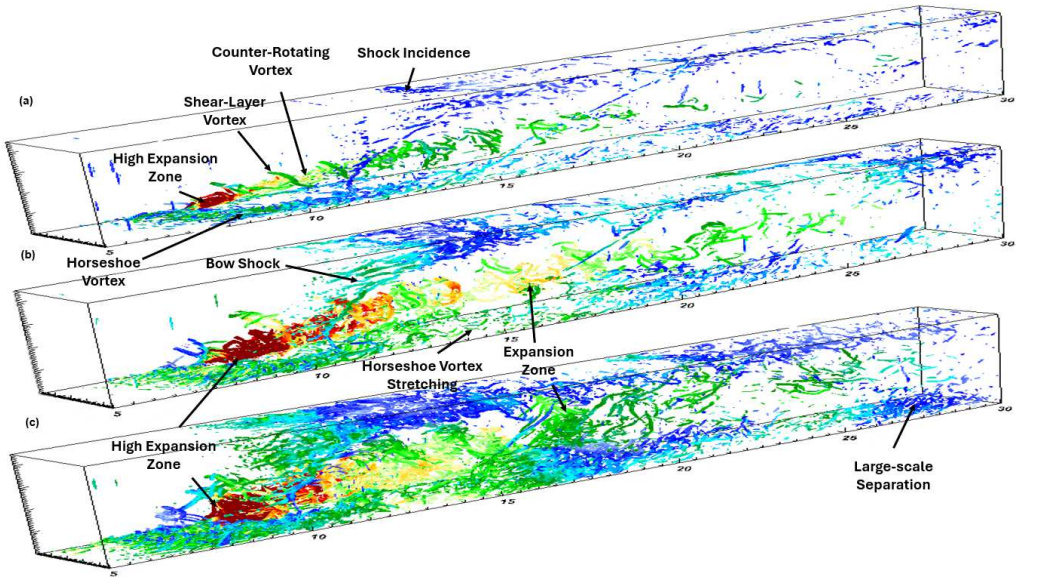


Figure 10: Instantaneous iso-surface of the vortical structure coloured by the local specific volume : (a) J=1.5, (b) J=3.0, and (c) J=5.87.

J=5.87 maintains a high level of organization, with the iso-surface persisting far downstream, indicating a more energetic and structurally robust vortex pair. The combination of higher core vorticity and sustained spatial coherence demonstrates that the jet-crossflow interaction at elevated J produces vortical structures that are not only stronger but also maintain their identity and influence over a much greater streamwise extent.

To analyze the behavior of the complex horseshoe vortex system, instantaneous streamlines originating from the central plane of the upstream and downstream recirculation zone are presented in Figure 9. The ability of the current simulation to resolve these structures is confirmed by the clear detection of multiple large-scale vortices, which is a known metric for adequate spatial resolution.

At the high momentum flux ratios investigated, the evolution of these vortices is evident. Notably, a portion of the hanging vortex—generated near the fuel injection point—is observed to merge with the pre-existing Vortex 1 and 2. The three vortices are generated between x=6.5 cm up to the injection point. The hanging vortex, which shelters the jet plume, is shed downstream and contributes to the formation of the counter-rotating vortex pair.

In Figure 10, the underexpanded jet generates a prominent expansion region within the incipient counter-rotating vortex pair (CVP). The spatial extent of this region in both the streamwise and lateral directions grows with increasing momentum flux, indicating enhanced vortex pair. The CVP is enveloped by the shear layer, which subsequently rolls up to form a distinct shear-layer vortex. The incident shock disrupts the wall boundary layer, producing zones of high compression followed by separation bubbles. At higher momentum flux ratios (J=3.0 and 5.87), the intensified shock strength leads to more pronounced boundary-layer separation. Furthermore, the footprint of the bow shock on the side and top walls is marked by the presence of these separation regions.

The expansion regions, previously identified in Figures 2, 3, and 4, are again evident in Figures 10a and b. Their persistence suggests they are primarily governed by the combustor geometry rather than the momentum flux ratio. That is, even at elevated injection pressures,

these expansion zones remain fixed in location, though they may become partially disrupted by the large-scale roll-ups of the shear layer, as seen in Figure 10c and 4.

The evolution of the horseshoe vortices follows a distinct pattern. Vortices 1 and 2 are split downstream and lifted upward, where they either contribute to feeding the CVP or amplify side-wall separation—a process observable by correlating Figures 7 and 10. Farther downstream, the increase in momentum flux also leads to the emergence of additional large-scale separation regions on both the upper and lower walls.

4.3. *Shock-Vortex Interaction*

Figure11 shows the interaction between the shock train and the vortical structures which are generated in the flow field for the three case studies at the downstream (x=12 to 35 cm). For the lowest J, the flow field for J=1.5 establishes a baseline of stable jet-crossflow interaction. The shock train, evident as coherent X-shaped structures in the schlieren images, remains largely undisturbed. The counter-rotating vortex pair and Kelvin-Helmholtz vortices in the shear layer, while present, are weak and lack the energy to significantly disrupt the compressible wave system. This is quantified by the dilatation fields (Fig. 11a), which reveal organized, quasi-two-dimensional bands of compression and expansion. Critically, at all three sampled heights—the near-upper-wall region (y=4 cm), mid-channel height (y=2.5 cm) and near the CVP core (y=1 cm)—the dilatation signal is periodic (a compression peak every 3-5 cm) and of low amplitude. This indicates that the shock waves can penetrate the weak vortex cores with only mild refraction, and the acoustic energy is distributed across resonant modes without a dominant frequency. This can explain the low- and moderate-frequency bands captured at the upstream pressure probe reported by Essa (2026). In this regime, the flow is stable, and the coupling between vortical and acoustic fields is weak.

At J=3.0, the system enters a transitional state where the intensified vortical structures begin to dominate the flow dynamics. The CVP gains significant strength, and large-scale KH roll-ups become pronounced features in the shear layer. The schlieren images show the shock train undergoing clear deformation—the once-clean X-shocks are now bent and smeared where they intersect the vigorous vortex cores. This deformation is a direct result of the shock-vortex interaction: the rotational core of a vortex presents a localized region of altered density, temperature, and velocity, effectively changing the local Mach number and causing the shock to bifurcate or refract strongly. The shock waves are no longer passive features but are actively sculpted by the vortical field. In this case, the CVP acts like a piston as they rotate and convect, they push and pull the fluids, and the flow shifts to be vortex dominated flow–this explains the emergence of a dominant mode in the moderate-frequency bands signifying the effect of the vortical structures in the flow field (Essa 2026).

The mechanistic details of this transition are captured in the dilatation field (Fig. 11b). A stark vertical stratification in flow unsteadiness becomes apparent. In the CVP core (y=1.0 cm), the signal is chaotic and energetic, filled with fine-scale fluctuations generated by intense rotation and strain. The shear layer (y=2.5 cm) shows larger-scale oscillations correlated with the passage of KH vortices. Most tellingly, these disturbances now penetrate to the near-upper-wall region (y=4.0 cm), where the dilatation signal, while still showing some periodicity, is visibly modulated. This vertical propagation of unsteadiness signifies that the energy from the vortex-dominated core is now feeding back onto the global shock system, forcing it into oscillation. This correlates precisely with the spectral data from the upstream probe, which shows the emergence of a dominant moderate-frequency mode (Essa 2026). This frequency is interpreted as the characteristic shedding frequency of the large-scale vortical structures as they interact with and modulate the shock train, representing a locked-in vortex-shedding mode that has become the primary organizer of the flow's unsteady energy. A similar behavior

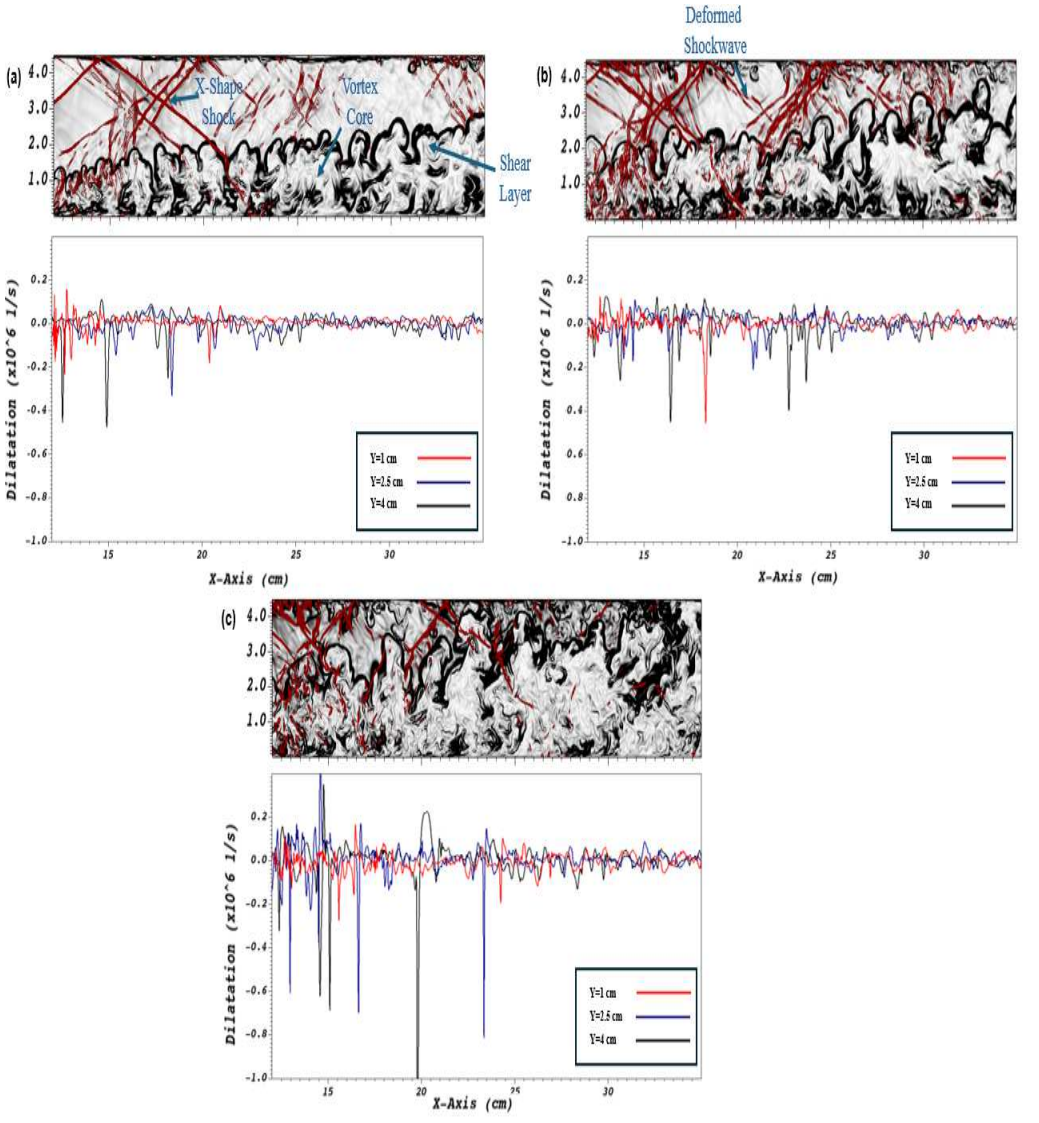


Figure 11: Instantaneous shock train-vortex interaction on the schlieren images and their dilatation fields ($\nabla \cdot \boldsymbol{u}$) with three analysis lines for (a) J=1.5, (b) J=3.0, and (c) J=5.87 at z= 2 mm. The lines are positioned to sample distinct flow regions: the near-upper-wall shock propagation zone (y=4.0 cm), the primary shear layer and KH instability region (y=2.5 cm), and the core of the counter-rotating vortex pair (y=1.0 cm).

of the shock-train was captured by exciting the downstream flow with a certain frequency to find that the shock-train responds with similar frequency values Xiong *et al.* (2018).

The flow at J=5.87 is characterized by the complete disintegration of the organized shock train, as visualized in the schlieren (Figure 11c). The CVP and associated vortical structures are now so powerful that they act as a distributed, unsteady blockage. The shock-vortex interaction progresses from deformation to termination; coherent shock waves cannot be sustained within the turbulent vortex cores. Instead of being refracted, the shocks are broken

down into a chaotic field of compression waves. The vortical energy has surpassed a critical threshold, overwhelming the flow's ability to maintain a coherent, global pressure separation.

The dilatation field for J=5.87 (Fig. 11c) is the clearest indicator of the fully developed global instability. The previously observed vertical stratification culminates in domain-wide chaos. The signals at all three heights—upper wall, shear layer, and CVP core—are saturated with high-amplitude, disorganized fluctuations. The clean, resonant acoustic waves seen at low J have been entirely replaced by a turbulent, multi-directional pressure field. Combining Figures 7 and 8, one can notice the deformation of the CVP, which supports the highly coupled shock-vortex structure following the findings of Wang *et al.* (2025). This is the visual manifestation of the shock-driven global mode described in Essa (2026). The flow is no longer composed of distinct vortices and shocks but is a fully coupled system where each component violently drives the other in a self-sustaining cycle.

The growth of large-scale Kelvin-Helmholtz waves with increasing momentum flux ratio deforms the bow and barrel shock structures (Figures 3 and 4). This deformation introduces significant nonlinearities upstream, feeding the global choking instability mode. Furthermore, higher momentum flux ratios enhance the spatial separation of KH waves on the windward side of the counter-rotating vortex pair (Xiao *et al.* 2024).

The parametric study from J=1.5 to J=5.87 reveals a systematic pathway to global instability, understood here through combined structural and nonlinear dynamical analysis. The sequence is as follows: increasing the jet momentum flux ratio strengthens the large-scale vortical structures, which interact with the shock train to generate intense, localized pressure fluctuations—quantified by the chaotic dilatation fields. This inherent unsteadiness is then potently amplified by the heat release from combustion, driving more violent interactions. The sustenance mechanism of the global mode can be described as: the mode is fed by nonlinear interactions upstream, achieves linear independence midstream, and regenerates nonlinearities downstream. The initial nonlinear interactions correspond to the region of most violent shock-vortex interplay, where energy is transferred into the nascent global mode. As the mode propagates, it achieves a coherent, self-sustaining state. Finally, upon interacting with downstream structures and the choking location, it triggers new nonlinear events, effectively closing a feedback loop where the large-scale mode regenerates the very disturbances that feed it. Thus, the vortex-shock interaction acts as a significant amplifier within a thermoacoustic cycle, where localized fluctuations lock into a domain-filling, low-frequency oscillation that dictates the system's dynamics.

This progression provides the fluid-mechanical context for the spectral evolution reported in Essa (2026). Initially, at moderate J, the flow is dominated by convective communications, where the passage of large-scale vortices generates a moderate-frequency signature. As the system approaches choking, this behavior transitions to a global mode. This global mode does not arise from a new source but emerges with significant magnitude because it is directly fed by the intense nonlinear interactions generated in the highly unsteady regions of shock propagation and vortex breakdown documented in this study. Thus, the violent vortex-shock dynamics are not merely a symptom but the essential nonlinear energy source that sustains the self-excited, domain-filling oscillation characteristic of the fully developed global instability.

To test the degree of coupling between the CVP core and the upper wall, cross-correlation analysis was performed between two pressure probes: one near the upper wall (x = 14 cm, y = 4 cm) and another inside the CVP (x = 10 cm, y = 2 cm), both on the central plane. It reveals a weak but statistically significant linear coupling ($|R|_{max} = 0.13$, $p << 0.01$) between CVP-core and near-wall pressure, with CVP-core leading by approximately 26 μs. This suggests that pressure disturbances propagate from the vortex core to the wall on acoustic timescales, though the weak correlation magnitude indicates this coupling plays only a secondary role in the global mode sustenance, which likely involves stronger nonlinear or multi-region

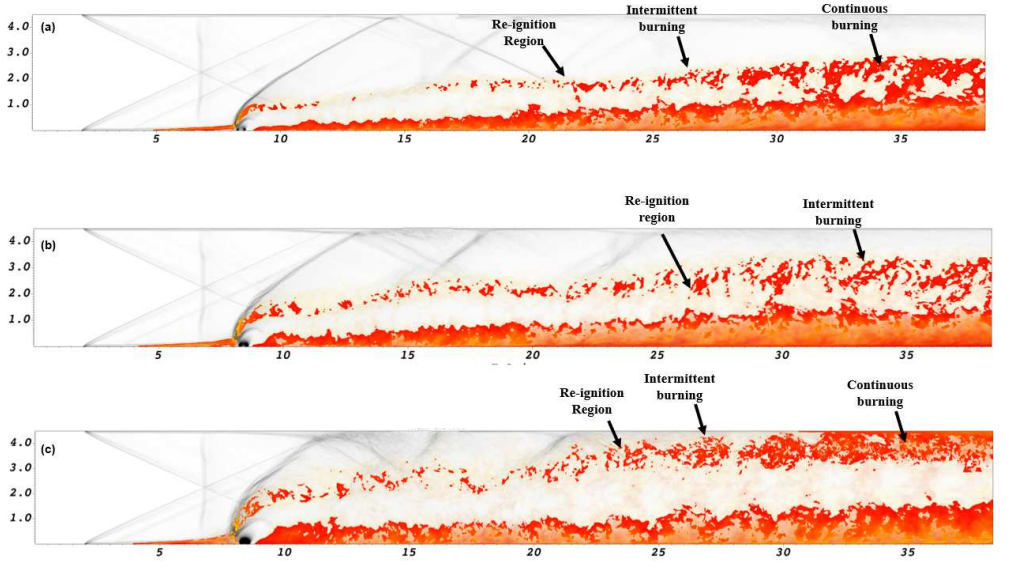


Figure 12: Time-averaged OH concentration between 1-1.5 ms using 27 samples: (a) J=1.5, (b) J=3.0, and (c) J=5.87.

interactions. Physically, this can be understood as the inability of the downstream supersonic flow to communicate directly with upstream regions; instead, feedback acoustic signals propagate through subsonic pathways established within the boundary layer and the CVP core.

5. Flame Anchoring and Quenching

5.1. *Anchoring and Shock-Induced Mixing*

The structure of the flame, characterized here by the OH radical distribution, aligns with established models for transverse jets in supersonic crossflow, where the flame anchors in regions of stabilized ignition and intense mixing (Gamba & Mungal 2015; Candler *et al.* 2017; Zhao *et al.* 2017). A key feature is the flame's concentration along the lower wall, a consequence of the shock train's dynamics. The system of compression waves and shocks effectively deflects the core flow downward, enhancing fuel-air mixing and creating a persistent, high-temperature region that facilitates flame anchoring on the wall. Simultaneously, the shear layer on the windward side of the counter-rotating vortex pair serves as a primary reaction zone, where the mixing rate is governed by the shear layer's intrinsic instability and the velocity differential between the fuel jet and the crossflow.

The concentration of the flame on the lower wall, evident in the time-averaged OH fields (Fig. 12), is a direct consequence of the three-dimensional shock structure documented in Figs. 2-4. The shock train, particularly the bow shock and subsequent compression waves, acts as a large-scale aerodynamic surface that deflects the supersonic crossflow downward. This global compression, which acts upon the entire flow field including the CVP visualized in Fig. 10, projects the core flow toward the lower wall to mix with the fuel, creating a persistent, high-pressure region ideal for sustaining combustion. This mechanism, which dominates over more localized shock-boundary-layer interactions, aligns with observations of wall-combustion in similar configurations (Gamba & Mungal 2015; Zhao *et al.* 2017). The resulting well-mixed, high-temperature zone provides a stable anchoring point for the

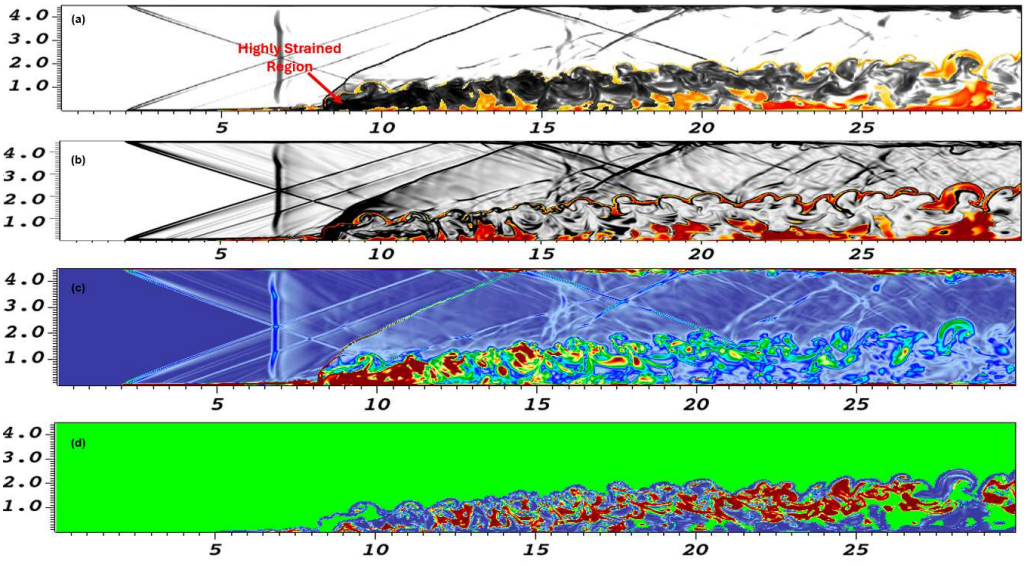


Figure 13: Instantaneous flames anchoring features of J=1.5: (a) Damkohler's number, (b) schlieren, (c) velocity gradient magnitude, and (d) Takeno flame index.

flame, as confirmed by the sustained high OH concentrations along the lower wall trajectory in all cases (Fig. 13b, 14b, and 15b).

Upstream of the injector, the flow separation induced by the jet obstruction plays a vital role in flame stabilization. The separation shock and the ensuing upstream recirculation zone (USR) create a low-velocity region that traps hot products and radicals, providing a continuous ignition source. This recirculation zone entrains a portion of the injected fuel, and the system of horseshoe vortices, previously detailed in Fig. 9, is instrumental in the mixing and transport process. These vortices efficiently mix the fuel with the decelerated flow within the boundary layer and subsequently convect the ignited mixture downstream, painting the flame along the lower wall and following the trajectory of the vortex legs. This mechanism establishes a robust flame-holding pathway that is distinct from the shear-layer-dominated combustion.

The present data provides a clear platform to address the longstanding discrepancy regarding the primary mechanism for local flame quenching. Gamba & Mungal (2015) attributed quenching to the interference of expansion fans which was introduced by the experimental setup, while Zhao *et al.* (2017) argued for high scalar dissipation rates due to local strain. Our results offer a synthesis that investigates these views by examining the coupled flowfield.

As shown in Fig. 10, the shear layer in all three cases is characterized by the presence of strong expansion regions. The underexpanded jet naturally generates these expansions, which are associated with high local velocity gradients. Crucially, by combining this observation with the vortical structures in Fig. 10 and 12, it becomes evident that these expansion zones coincide with the cores of the most intense vortical activity—the Kelvin-Helmholtz rollers and the windward side of the CVP.

The longstanding discrepancy regarding the primary mechanism for flame quenching in supersonic transverse jets—whether dominated by expansion fan interference as argued by Gamba and co-workers (Gamba *et al.* 2011, 2012; Gamba & Mungal 2015) or by high scalar dissipation rates due to strain as proposed by Zhao et al. (Zhao *et al.* 2017)—is critically

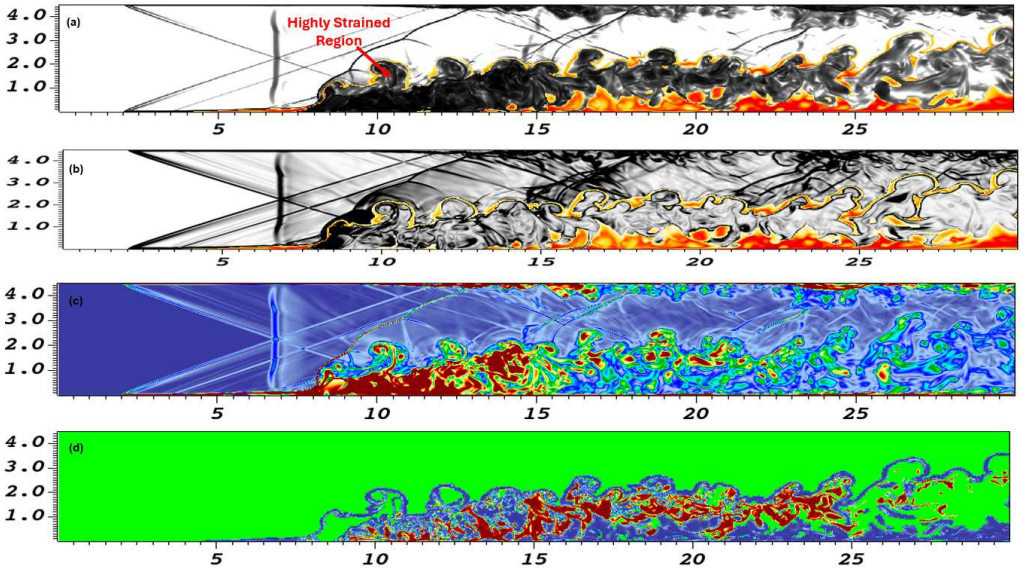


Figure 14: Instantaneous flames anchoring features of J=3.0: (a) Damkohler's number, (b) schlieren, (c) velocity gradient magnitude, and (d) Takeno flame index.

re-examined here through a multi-diagnostic analysis. The present study bridges this divide by revealing that the two mechanisms are not mutually exclusive but are intrinsically coupled through the flow's vortical dynamics. Figures 10 and 12 demonstrate that the shear layer in all cases coincides with prominent expansion regions, as outlined structurally in subsection 4.1. The underexpanded jet inherently generates the first expansion region downstream of the barrel shock, establishing regions of high velocity gradient between the jet and the crossflow. However, the expansion alone does not fully account for the observed quenching patterns.

To move beyond qualitative attribution, the combustion regime was systematically characterized using the Damkohler number (Da), the ratio of mixing to chemical time scales, alongside the Takeno Flame Index and velocity gradient fields. For the lowest momentum flux ratio, J=1.5 (Fig. 13), the Damkohler map reveals persistently low Da values within the core of the counter-rotating vortex pair (CVP), indicating regions where chemical kinetics are too slow relative to mixing, leading to unburned mixtures. This is compounded by a local equivalence ratio exceeding the upper flammability limit ($\phi > 2.5$) for hydrogen-air mixtures (Glassman *et al.* 2014). Consequently, the CVP core remains largely devoid of significant reaction, as evidenced by the sparse OH distribution. The shear layer thickens downstream (Figs. 13b,c) as jet energy is converted into rotational energy within the CVP, reducing the velocity gradient and creating a more favorable environment for flame propagation. The Takeno Flame Index (Fig. 13d) confirms this region is dominated by non-premixed combustion.

The flow at J=3.0 marks a critical transition where the mechanism of quenching becomes unequivocally linked to the strain field. Figure 14a reveals that the large-scale Kelvin-Helmholtz (KH) rollers are characterized by very low Damkohler numbers. This directly correlates with the intense velocity gradients localized within the expansion zone of the shear layer, as shown in Fig. 14c. Here, the expansion region, a consistent feature of the flow (Fig. 10), generates an extremely high local velocity differential. This drastically reduces the mixing time scale ($\tau \propto |S|^{-1}$), driving Da below unity and leading to flame extinction via excessive strain—a finding that provides direct support for the dissipation-based quenching

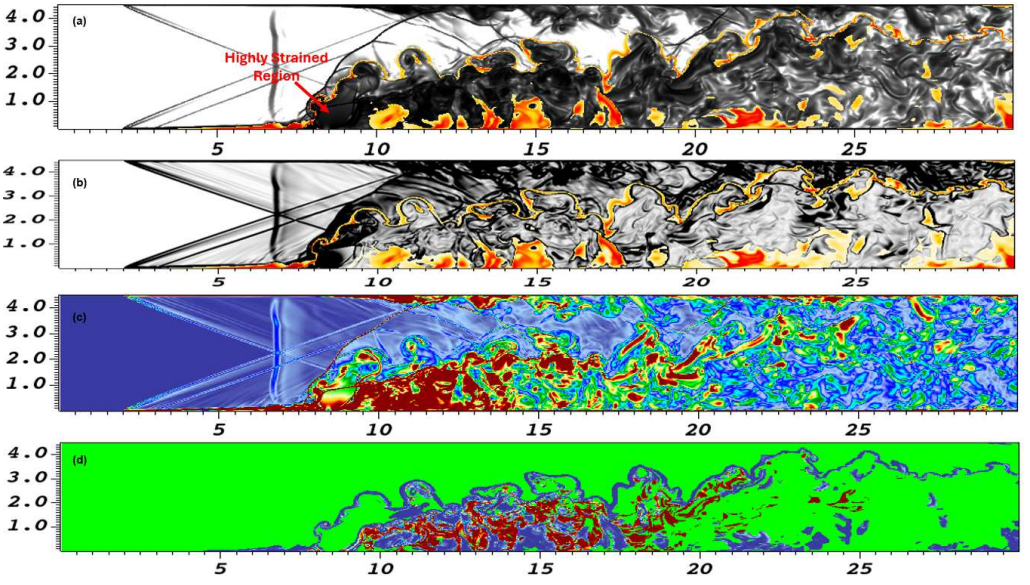


Figure 15: Instantaneous flames anchoring features of J=5.87: (a) Damkohler's number, (b) schlieren, (c) velocity gradient magnitude, and (d) Takeno flame index.

mechanism proposed by Zhao *et al.* (2017). The increased size and energy of the vortical rollers at this condition serve to intensify and broaden this high-strain region. This explains the pronounced spatial intermittency observed in the time-averaged OH field between x=10–40 cm (Fig. 12b), a stark contrast to the more continuous flame sheet re-igniting downstream at lower J. Furthermore, the Takeno Flame Index (Fig. 14d) confirms that the dominant combustion mode under these conditions is non-premixed, consistent across all three cases studied.

The highest momentum flux ratio case, J=5.87, presents a more complex scenario where the expected trends are modulated by strong confinement effects. As predicted, the region of high strain expands with the growing CVP. Unexpectedly, however, Fig. 12c shows that a continuous flame regime re-establishes in the shear layer downstream of x=20 cm. This revival is a direct consequence of confinement: the lateral walls constrain the flow, limiting the lateral growth of the CVP and enhancing near-wall mixing and recirculation, which re-energizes the flame. Despite this, the underlying local extinction mechanisms remain active. The Damkohler map (Fig. 15a) and velocity gradient field (Fig. 15c) confirm that pockets of high strain and chemically controlled flow ($Da < 1$) persist and are responsible for the streamwise modulation of the flame, including local extinctions along the otherwise flame-anchored lower wall.

The analysis is deepened by examining the chemical heat release and key radical species. The spatial distribution of heat release rate, visualized on Q-criterion iso-surfaces in Fig. 16, confirms the horseshoe vortices as primary exothermic reaction zones. In contrast, the CVP cores exhibit only sporadic heat release, consistent with their high-strain, mixing-limited nature. A significant thermochemical effect observed with increasing J is the dissociation of oxygen molecules into atomic oxygen (O) and ozone (O_3) within the separation bubbles induced by strong shock waves on the upper wall. This endothermic dissociation process acts as a local thermal sink, absorbing energy from the flow as a direct result of the intense shock heating and pressure rise. While this thermal sink does not directly cause the shear-layer quenching, it represents an important competing energy pathway that can influence

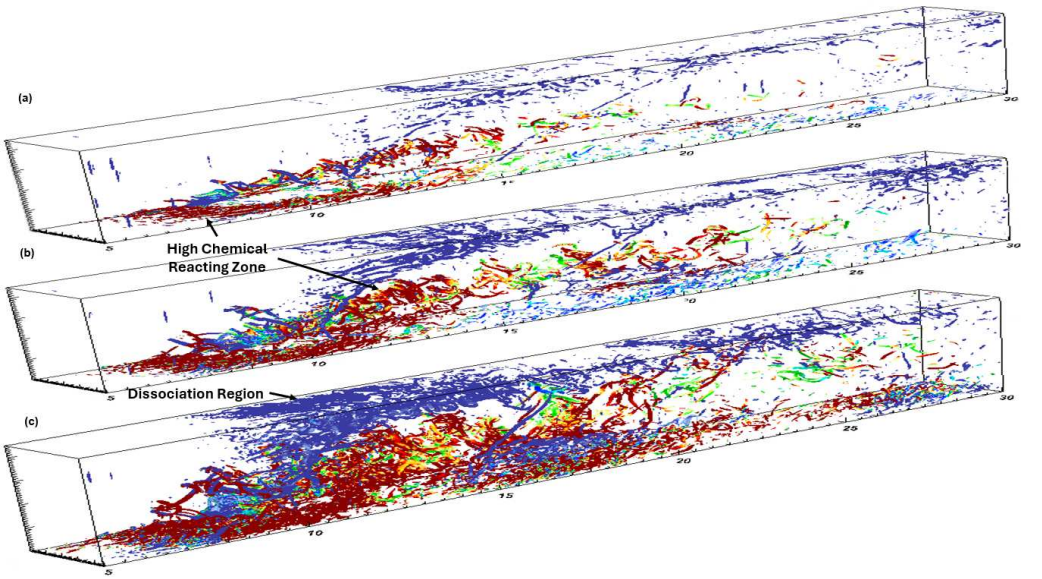


Figure 16: Instantaneous iso-surface of the vortical structure coloured by the local heat release rate : (a) J=1.5, (b) J=3.0, and (c) J=5.87.

the overall combustion efficiency and temperature field, particularly in the confined, high-pressure environment of the present configuration.

Figure 17 shows the Q-criterion colored by the local HO_2 mass fraction. The vortex cores sustain the highest concentrations of HO_2, a species central to chain-termination reactions that compete with the chain-branching reactions responsible for flame propagation (Glassman *et al.* 2014). The presence of elevated HO_2 signifies a shift in the local chemical pathway from vigorous oxidation (producing OH and O) to a slower, terminating sequence. By overlaying this information with the heat release distribution (Fig. 16), a direct correlation emerges: regions identified as quenched or weakly reacting coincide with areas of high HO_2 concentration embedded within the high-strain vortex cores.

The present results necessitate a reassessment of the role attributed to expansion fans in flame quenching. Gamba & Mungal (2015) identified a prominent expansion fan, generated by a compression ramp inlet, as the primary cause of local extinction. However, the data from this confined configuration—which lacks such an inlet feature but still exhibits strong expansion regions due to the underexpanded jet and channel flow (Fig. 10)—reveals a more fundamental mechanism. Quenching consistently correlates not with the expansion itself, but with regions of intense vorticity and high strain that are spatially coincident with these expansions. This is evidenced by the direct mapping of low Damkohler numbers to high velocity gradients within vortex cores and shear layers (Figs. 13–15), and by the chemical fingerprint of chain termination (elevated HO_2) in these same regions (Fig. 17).

This suggests that in Gamba's experiments, the expansion fan was likely a conspicuous marker for a zone of high shear and vortex activity, rather than the direct extinguishing agent. The expansion may have facilitated quenching by creating a favorable thermodynamic environment (reduced temperature and pressure), but the sufficient cause was almost certainly the high scalar dissipation rate generated by the associated strain field—a mechanism consistent with the arguments of Zhao *et al.* (2017). Thus, the expansion fan's role is secondary and conditional; it is the vortex-enhanced strain within such regions that acts as the universal extinction agent.

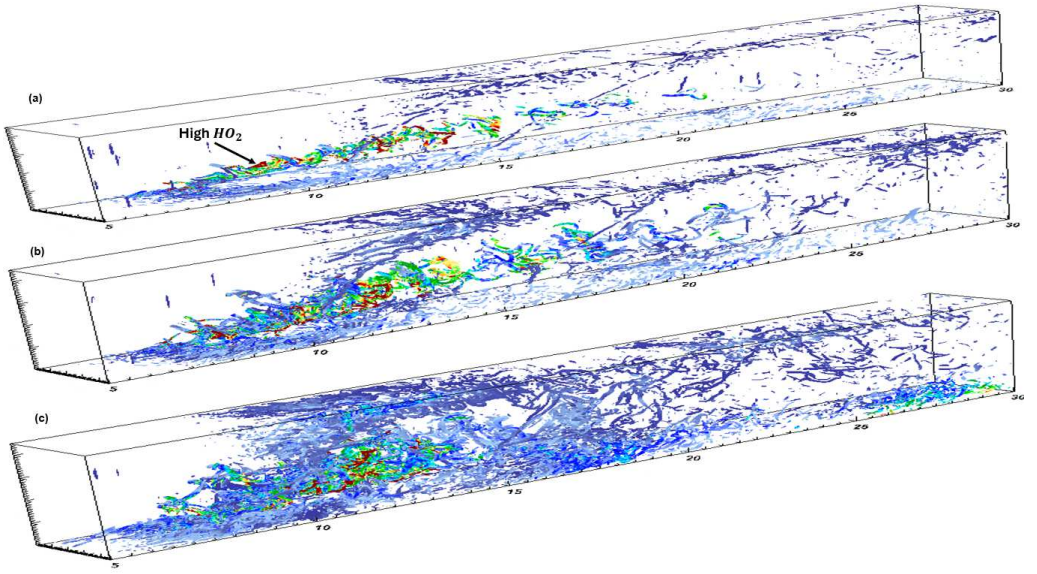


Figure 17: Instantaneous iso-surface of the vortical structure coloured by the local HO_2 mass fraction : (a) J=1.5, (b) J=3.0, and (c) J=5.87.

In conclusion, this study advances the quenching debate by decoupling correlation from causation. While expansion regions—whether from inlet ramps or underexpanded jets—are common sites for flame quenching in supersonic crossflows, they are not the primary cause. The fundamental mechanism is excessive strain leading to high scalar dissipation, which disrupts the flame's radical pool and drives the chemistry toward termination pathways, as indicated by HO_2 buildup. This strain is predominantly generated and sustained by the intense vortical structures (CVP, KH rollers) that develop in these complex flow regions. Therefore, a unified model emerges: large-scale flow features (e.g., shocks, expansions) define susceptible zones, but it is the fine-scale, vortex-driven strain within these zones that executes local extinction. This framework reconciles the observations of both Gamba et al. and Zhao et al., elevating the understanding of quenching from a geometry-specific explanation to a fluid-chemical framework.

5.2. *Evolution of Flame-Holding Topology with Momentum Flux*

Figure 18 shows the OH distribution in several lateral planes for J=1.5. Near the injector, flames are distributed continuously along the lower wall but avoid the lateral separation wing. The mixture is ignited by compressive heating across the collision shock; however, within the separation region, the equivalence ratio rises above the rich flammability limit ($\phi > 2.5$), preventing sustained combustion—a manifestation of rich-limit suppression. Vigorous re-ignition occurs in the reattachment valley, sustaining wall-attached burning downstream (Fig.18a). Regions of intense OH (reddish hues) trace the coherent branches of the HSV, indicating efficient fuel transport and mixing along these structures.

Within the DSZ, despite high strain rates around its periphery, combustion proceeds robustly with no apparent quenching. OH concentrations remain high ($Y_{OH} > 0.02$) even in regions of elevated velocity gradient, indicating that at low J, flammable mixtures persist in the DSZ and are not extinguished by the local strain—a regime of strain-tolerant rich combustion.

Farther downstream, burning occurs predominantly in excessive fuel-rich regions ($\phi > 2.5$)

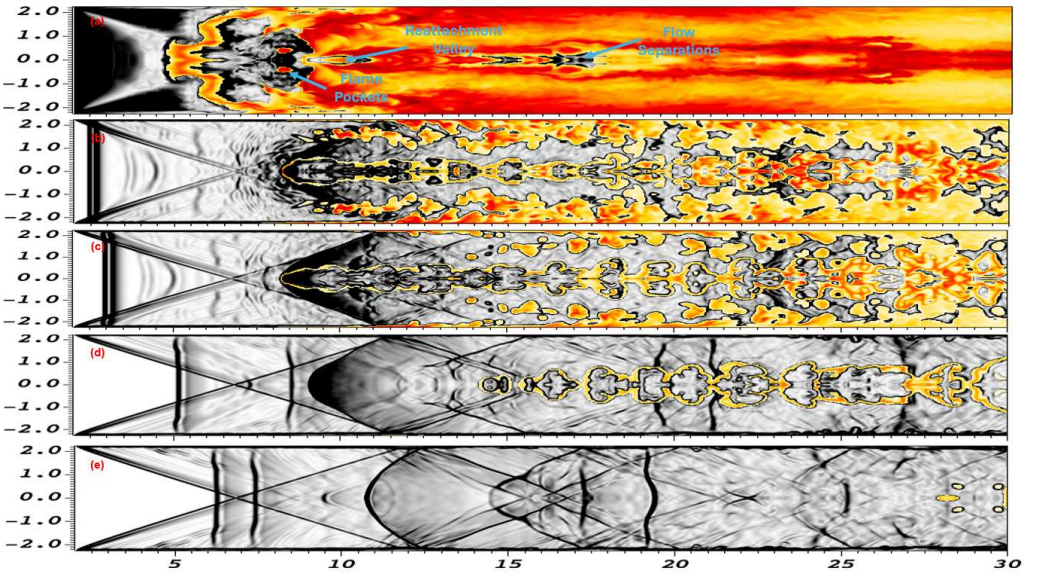


Figure 18: Instantaneous OH mass fraction in the lateral plane of J=1.5: (a) y≈44 microns, (b) y=0.25 cm, (c) y=0.5 cm, (d) y=1.5 cm, and (e) y=2.5 cm.

where strain is low. Although some localized burning persists in high-strain zones, the flame is largely absent in regions of extreme velocity gradient, indicating that strain-induced extinction becomes dominant where mixtures remain flammable but strain rate exceeds the local flame extinction limit. This downstream behavior highlights the spatial decoupling of mixture- and strain-limited combustion at low J.

Moving away from the wall (Fig. 18b,c), OH concentrations diminish, reflecting weaker combustion activity in the outer shear layers and minimal burning along the sidewalls. However, at an intermediate height (y=0.25cm), the sidewalls sustain combustion due to the vortical transport mechanism of the lifted HSV branches, which advect hot products and radicals into the near-wall region. The collision shock continues to provide a favorable high-pressure, high-temperature environment for ignition where the mixture is sufficiently prepared.

In the farthest slices from the lower wall (Fig. 18d,e), the flame becomes almost entirely confined to the windward shear layer. In this stable (J=1.5) configuration, the flow is dominated by coherent shock structures, with combustion largely decoupled from the wall and sustained by shear-layer mixing.

At J=3.0, the flame-holding topology transitions markedly from the lower-J case. The two side flame pockets observed at J=1.5 now multiply into four distinct ignition kernels: two positioned ahead of the injector and two immediately downstream of it (Fig.19a). This flame spreading coincides with a significant redistribution of reaction zones. While OH remains intense along the central plane and traces the intensified horseshoe vortex, the downstream recirculation zone (DRZ) now sustains only weak oxidation: its interior is filled with cold, over-rich hydrogen ($\phi > 2.5$) and exhibits low OH concentrations ($Y_{OH} < 0.015$), indicating partial oxidation in non-flammable mixtures. In contrast, high-strain regions around the DRZ periphery support intense flames ($Y_{OH} > 0.025$), demonstrating that combustion can persist in high-shear zones when mixtures remain within the flammable range.

Farther downstream, moderate to high strain rates coincide with over-rich mixtures ($\phi >$ 2.5), yielding low OH concentrations—a regime where strain and over-richness jointly

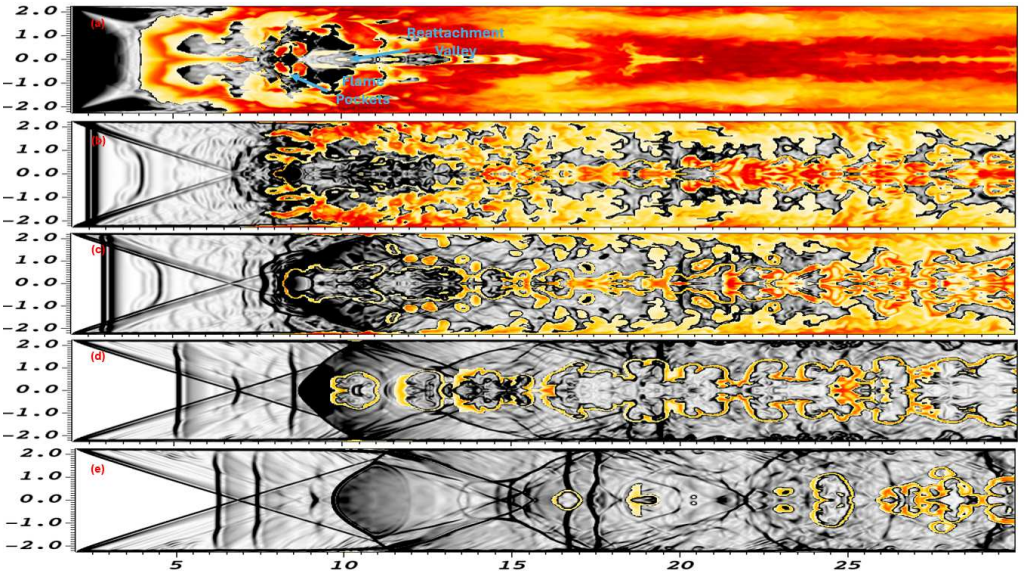


Figure 19: Instantaneous OH mass fraction in the lateral plane of J=3.0: (a) y≈44 microns, (b) y=0.25 cm, (c) y=0.5 cm, (d) y=1.5 cm, and (e) y=2.5 cm.

suppress flame development around the central plane (Yellow regions). This contrasts with the low-J case, where rich mixtures in low-strain zones burned robustly. Thus, at J=3.0, the flame structure reflects a transitional state: mixing is enhanced (producing more ignition kernels), yet the resulting over flammability limit pockets and elevated strain begin to compete, leading to localized extinction in regions that were fully reactive at lower J.

The HSV structure itself becomes more chaotic and spatially extended (Fig.19b,c), reflecting the stronger jet–crossflow interaction. This enhanced vortical activity improves near-wall mixing, yet it also introduces higher local strain, which may contribute to the local extinction within the DSZ. Downstream of the injector, the flame does not exhibit large-scale quenching; however, the highest OH concentrations remain tightly organized around the centerplane ($Z \approx 0$), suggesting that the core of the flow—guided by the HSV and central shear layer—retains the most favorable mixing and chemical timescales for sustained combustion. The lateral spread of combustion is thus limited, with the intense reaction zone anchored centrally rather than distributed across the span as the OH intensity decreases between the central plane and the side walls.

This case represents a transitional regime where increased jet penetration and vortical strength disrupt the wall-dominated combustion of J=1.5, extinguish the DSZ anchor, and consolidate the flame into a more centralized, vortex-guided structure with multiple discrete upstream ignition sites.

At J=5.87, the horseshoe vortex becomes a highly efficient mixing mechanism, spreading ignited mixture across nearly the entire lower wall. This is evident from the widespread reddish OH coloration along the wall surface (Fig. 20a). However, distinct dark spots—regions of local flame extinction—persist in the wakes, flow separation zones, and within the downstream recirculation zone itself. Near the injector, the previously isolated flame pockets have now merged into a continuous region of burned mixture. A faint reignition zone is again visible in the reattachment valley, indicated by a very light yellow color.

Within the DSZ, OH is largely confined to the periphery; the interior shows only faint OH ($Y_{OH} < 0.015$) despite low local strain, indicating that the mixture is over-rich ($\phi > 2.5$)

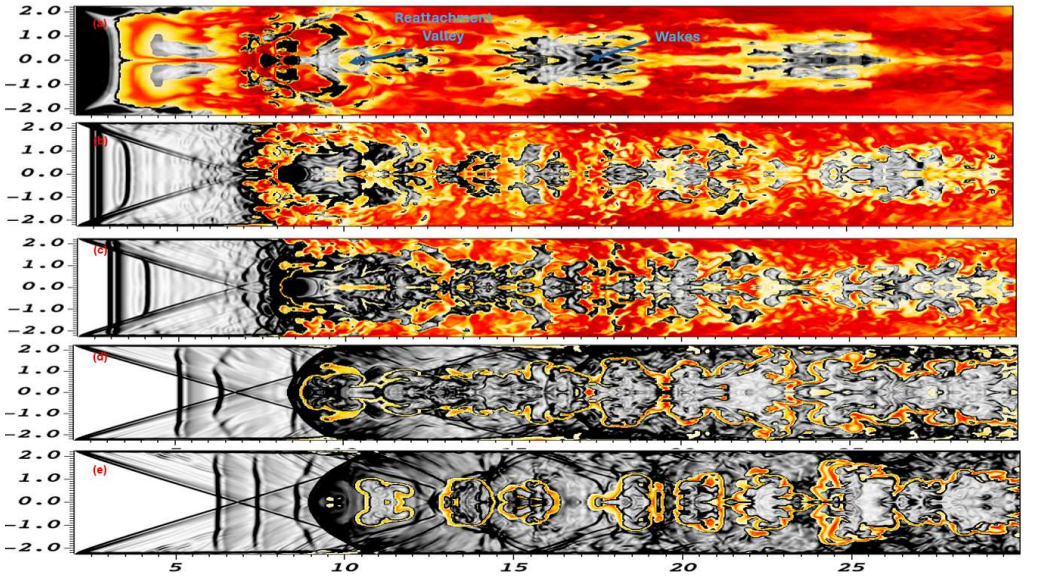


Figure 20: Instantaneous OH mass fraction in the lateral plane of J=5.87: (a) y≈44 microns, (b) y=0.25 cm, (c) y=0.5 cm, (d) y=1.5 cm, and (e) y=2.5 cm.

and non-flammable—a clear case of rich-limit suppression. Notably, high-strain regions around the DSZ no longer sustain the intense flames seen at lower J; instead, moderate OH levels (0.015–0.03) appear only where strain remains moderate, underscoring the growing dominance of mixture-driven rather than strain-driven extinction at this momentum flux.

By correlating the flame structure (Fig. 20a) with the shock topology (Fig. 4a), a direct link between compressible dynamics and local quenching becomes clear. The dark flame spots align spatially with locations where deformed or deflected shockwaves or strong compression waves intersect the lower wall. These shock interactions disrupt the coherency of the CVP, generating highly chaotic regions and imposing intense local strain. It is within these high-strain, shock-induced CVP transverse compression creating a high-strain over-rich mixture regions that the flame is consistently extinguished with a low concentration of transported highly reactive radicals to this region.

Confinement plays a defining role in the J=5.87 case, sustaining strong near-wall combustion (Fig. 20c,d) that exceeds levels seen at lower J. This is attributed to two compounding mixing mechanisms: (1) the active convection of hot, radical-rich gases from upstream regions, and (2) enhanced fuel-air entrainment in the downstream separation zone, where fuel withdrawn into the recirculation mixes with oxidizer deflected leeward of the counter-rotating vortex pair by the combined action of the bow shock and the shock train.

The shear layer is distinctly visible at y=1.5 cm and 2.5 cm (Fig. 20d,e). Its thickness evolution—narrowing near the injector and broadening downstream—aligns with the time-averaged OH distribution (Fig. 12c) and follows the streamwise flame development discussed earlier. Notably, flame is also anchored within the sidewall boundary layers between x=14 cm and 16.5 cm, a direct consequence of vortical transport. This sidewall combustion is sustained by vortices generated in the early to mid-portions of the upstream recirculation zone, which redistribute hot products and fuel toward the sidewalls.

Figure 21 presents a critical spanwise-normal (YZ-plane) view of the instantaneous OH distribution at multiple streamwise locations, revealing the three-dimensional flame-holding architecture and its evolution with momentum flux ratio J. When interpreted alongside

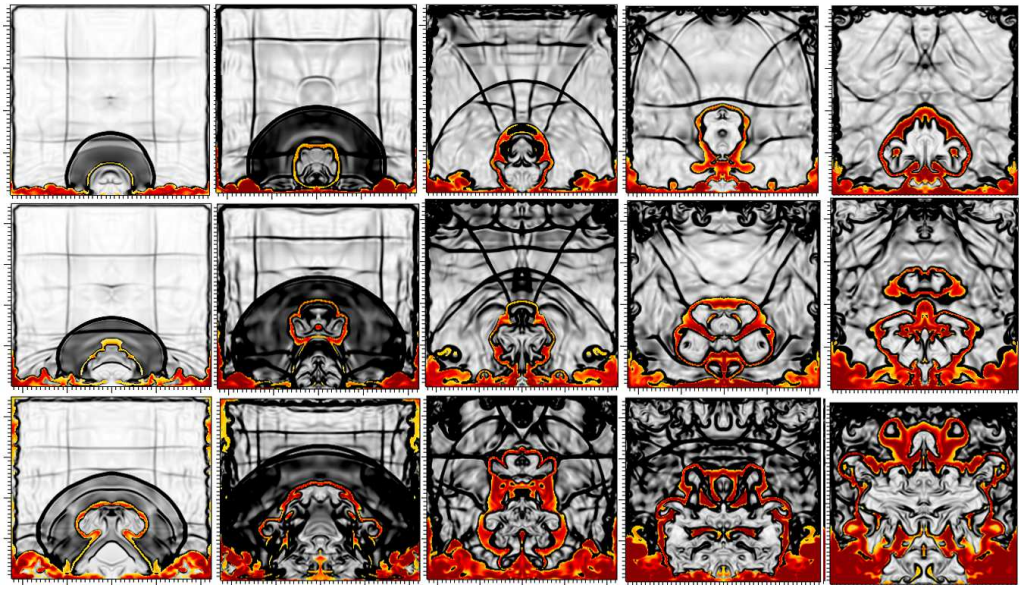


Figure 21: OH mass fraction for different momentum flux ratio (J=1.5, 3.0, and 5.87) and slices in the lateral direction (YZ-plane) downstream the injector (x=9, 10, 15, 20, and 25 cm): J increases from the top to the bottom, and x increases from left to right.

the lateral schlieren images in Figure 9, these slices disentangle the roles of compressible dynamics and vortical transport in shaping the flame topology.

At J=1.5 (top row), the flame is predominantly concentrated near the lower wall and around the shear layer. The OH distribution is compact, with relatively limited spanwise spread, consistent with a relatively weak jet-crossflow interaction. The shock structure in corresponding Figure 7 slices is organized and coherent, with minimal disruption from vortical structures. There is no evidence of sustained combustion on the sidewalls or upper regions; flame holding is largely confined to the upstream recirculation zone, the lower-wall, shear layer, and the downstream recirculation zone. The observed flame topology—including the continuous lower-wall burning and the upstream flame holding—is organized by the coherent, less energetic horseshoe vortex, which promotes near-wall mixing but does not drive any combustion into the upper sidewall regions.

The transitional case J=3.0 (middle row) exhibits a clear shift toward three-dimensional flame anchoring. Prominent flame pockets appear on the sidewalls in the near-field (x=9-10 cm), a feature absent at J=1.5. This is attributed to the stronger bow shock, which now significantly disrupts the sidewall boundary layers, enhancing local mixing and creating pockets where mixture can ignite. These sidewall flames are fed by vortices V1 and V2 shed (Fig. 9b) from the intensified upstream recirculation zone, which transport reactive mixture laterally toward the walls. Further downstream (x=25 cm), elevated OH concentrations are observed at the lower sidewall corners. This is consistent with the stretching and eventual impingement of the horseshoe vortex legs as they convect downstream, trapping hot products in the corner regions.

The shear layer also begins to play a distinct role. Kelvin-Helmholtz rollers emerge as coherent flame-holding structures, sustaining reaction zones along their edges as part of the developing shear layer. Meanwhile, a well-defined reaction zone persists around the periphery of the counter-rotating vortex pair, indicating continued combustion in the core of the jet-crossflow interaction, but it is modulated by increased strain.

Thus, at J=3.0, the flame begins to decouple from a purely lower-wall anchored configuration. The stronger shock–boundary-layer interaction and the more energetic upstream vortex shedding work in concert to distribute combustion onto the sidewalls, both in the immediate wake of the jet and in the downstream corners. The flame transitions from a wall-dominated to a multi-layered structure. Combustion is simultaneously sustained by: (1) shock-enhanced sidewall pockets, (2) shear-layer KH rollers, (3) the CVP peripheral reaction zone, and (4) downstream HSV-driven corner burning. This reflects the more distributed, vortex-mediated stabilization emerging at this intermediate momentum flux.

The most striking behavior is observed at J=5.87 (bottom row). Here, prominent flame-holding regions appear on the upper sections of the sidewalls, particularly in the near-field slices (e.g.,x=9-15cm). This phenomenon is a direct consequence of the intensified bow shock. The stronger bow shock significantly increases pressure and temperature along the sidewalls, enhancing boundary-layer mixing and creating thermochemical conditions favorable to ignition and stabilization. The schlieren images (Fig 7) for J=5.87 show these shock waves impinging directly on the sidewalls, coinciding spatially with the OH pockets (Fig. 21).

Furthermore, the complex HSV system plays a dual architect role. Its lifted and split branches, generated upstream, act as coherent conduits. They transport radical-rich, burned mixtures from the central injection region laterally and upward, directly feeding not only the lower-wall flame but also supplying the sidewall combustion zones and enriching the counter-rotating vortex pair with hot products. This vortical supply network ensures that the CVP core, while often strain-limited, is periodically replenished with reactive mixture, moderating local extinction.

5.3. *Quantitative Regimes of Flame Survival and Extinction*

To resolve the competing explanations for local flame quenching and to establish a quantitative basis for the observed flame topology, we perform a joint statistical analysis of the coupled strain-thermochemistry fields for the supercritical case (J=5.87). Figure 22 bridges the governing variables: the thermodynamic state (pressure), chemical activity (OH radical concentration), and the local mixing intensity (strain rate magnitude, $|S|$). By contrasting the near-wall plane with the central transverse plane (z=0), the analysis delineates the distinct combustion regimes responsible for flame withholding in sheltered zones and extinction in exposed, high-strain regions.

The scatter plots reveal two principal determinants for local flame survival: (1) a strain rate threshold, above which reactions are extinguished irrespective of pressure, and (2) a pressure threshold (< 2 bar), below which combustion is suppressed even at moderate strain. The intersection of these criteria—low strain and high pressure—defines the 'safe zone' for sustained burning, which the flow architecture selectively provides in shock-compressed near-wall layers and within the braids of large-scale vortices.

The fundamental trend—OH concentration decreases monotonically with increasing strain rate—is evident in both planes, confirming high scalar dissipation as a primary extinction mechanism. This relationship is not merely correlative; the data reveals a sharp suppression of chemical activity beyond critical strain thresholds, which coincide with regions of elevated vorticity, confirming vortex cores as the direct seats of quenching.

In the central plane (Fig. 22c), OH concentration begins to decline at a relatively low strain rate ($|S| \approx 10^6 s^{-1}$, corresponding to vorticity $\omega \approx 4 \times 10^5 s^{-1}$). This threshold represents only 8% of the maximum strain recorded in this plane ($1.3 \times 10^7 s^{-1}$). Beyond this value, combustion persists only in weakened form ($Y_{OH} < 0.03$), and the scatter plot shows a pronounced void where high strain ($|S| > 4 \times 10^6 s^{-1}$) completely extinguishes the flame.

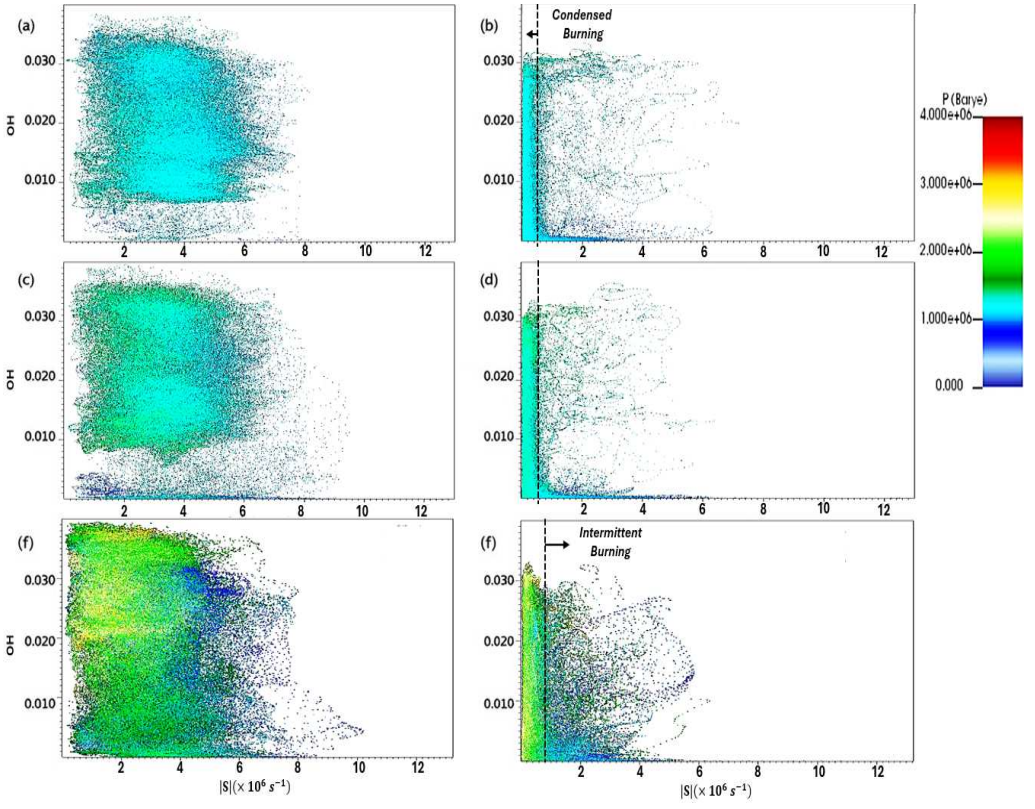


Figure 22: Scatter plot of the OH concentration with the strain rate based on their maximum values at different planes coloured by pressure: (a) transverse plane (z=0) of J=1.5, (b) transverse plane (z=0) of J=3, (c) transverse plane (z=0) of J=5.87, (d) lateral plane (y≈ 44μm) of J=1.5, (e) lateral plane (y≈ 44μm) of J=3, and (f) lateral plane (y≈ 44μm) of J=5.87.

The central plane of the lower J values experienced the almost same behavior of the highest momentum flux ratio case (J=5.87), as show in figures 22a-b.

In stark contrast, the near-wall layer exhibits a fundamentally different combustion regime. Flames persist within intense vortical structures such as the HSV despite strain rates exceeding $|S| \approx 5.2 \times 10^6$ s^{-1}. The HSV acts as a flame-holding region not because it is fuel-rich, but because it is a high-mixing, near-stoichiometric zone where fuel is rapidly entrained and consumed, leading to a robust combustion even under high shear. This regime explains the survival of reaction in high-strain zones that would quench stoichiometric mixtures in the central plane. Flame anchoring here is enabled by two complementary effects: (1) intense mixing that maintains a near-stoichiometric mixture in the HSV, and (2) the acceleration of chemistry due to high compression regimes. Unlike the central plane, where low-OH zones arise from strain-limited extinction, near-wall dark spots coincide with over-rich, poorly mixed pockets ($\phi >> 2.5$) that remain non-flammable even at high temperatures (> 1500 K)—a manifestation of mixture-limited suppression rather than aerodynamic quenching. Notably, these dark spots along the lower-wall central plane ($Z \approx 0$) originate from separation zones that entrain hydrogen from the CVP, creating locally over fuel-rich regions that are starved of oxidizer and thus cannot ignite.

The thermodynamic state, dictated by the shock train, is equally decisive. High OH

concentrations ($Y_{\mathrm{OH}} > 0.02$) are exclusively associated with compressed regions ($P > 2$ bar) in the central plane, where elevated pressure and temperature extend the rich flammability limit, permitting combustion even at $\phi > 2.5$. Low-OH zones reside in expansions and in fuel-rich regions where mixing is insufficient to bring the local equivalence ratio into a flammable range. This direct link between shock compression and enhanced combustion explains the counter-intuitive early shear-layer re-ignition observed at $J = 5.87$ compared to $J = 3.0$: stronger shock compression at the higher J can locally overcome mixing-limited extinction, shortening the extinction length.

For the near-wall layer, the requirement is more stringent: intense reactive zone ($Y_{OH} > 0.03$) demands both high compression ($P > 2.5$ bar) and low-to-moderate strain ($|S| < 4.2{\times}10^{6} s^{-1}$). High pressure is thus a necessary, but insufficient, condition. This is exemplified downstream of the reattachment valley (Fig. 20a). Between x=15-20 cm, where the pressure rises to approximately 3 bar, an 'inactive combustion island' is observed—a region meeting the pressure criterion but devoid of OH due to its location within an over fuel-rich separation zone (Fig. 6c). Conversely, the reattachment valley itself, with lower pressure (1.5-2 bar), shows only weak combustion.

Finally, a systematic evolution in the low-OH ($Y_{\mathrm{OH}} < 0.01$) population with increasing momentum-flux ratio was observed. For $J = 1.5$, almost no cells exhibit $Y_{\mathrm{OH}} < 0.008$; the OH field is dominated by moderate-to-high values, indicating widespread combustion. At $J = 3.0$, a distinct population of low-OH cells ($Y_{\mathrm{OH}} < 0.002$) emerges, signifying the onset of localized extinction events in regions where strain and over-rich mixtures jointly suppress reaction. For $J = 5.87$, low-OH cells become abundant and span a continuous range ($0 < Y_{\mathrm{OH}} < 0.01$), filling the gap observed at lower J. This continuous low-OH scatter reflects the fragmented, highly intermittent combustion characteristic of the high-J regime: vigorous vortical mixing creates numerous fuel-rich pockets that either burn weakly or not at all, while simultaneously generating strain rates that quench any lean or near-stoichiometric mixtures.

6. Conclusion

This study of a sonic hydrogen jet in a supersonic crossflow has systematically elucidated the interplay between shock-vortex dynamics and flame stabilization/extinction, advancing a unified model for supersonic combustion in confined transverse jet configurations.

At low J, the flow is characterized by coherent shock trains and weak vortical structures, sustaining predictable compression and orderly wave propagation. As J increases, the intensification and redistribution of vortical energy—marked by the disproportionate growth of the secondary anticlockwise trailing vortex pair relative to the primary CVP—drives a nonlinear restructuring of the flow. Moderate J regimes exhibit intensified counter-rotating vortex pairs and Kelvin–Helmholtz rollers that deform the shock train.

At high J, the system undergoes a regime transition: the vortical structure expands spatially (Fig. 11), acting as a dynamic, piston-like obstruction that significantly enhances flow blockage. The resulting violent shock-vortex interaction dismantles the global pressure separation and generates chaotic dilatation fields, leading to system-scale instability.

Thus, vortex-shock coupling is identified as the primary nonlinear energy source for large-scale compressible unsteadiness in this configuration, with the CVP transitioning from a passive mixing structure to an active, piston-like driver that modulates the entire wave system. Cross-correlation analysis quantitatively confirms this role: pressure disturbances within the CVP lead those at the upper wall by 26 μs ($R = 0.13$, $p < 0.01$), demonstrating that the CVP actively participates in the acoustic feedback loop sustaining the global instability.

Increasing J transforms the flame from a two-dimensional, wall-attached sheet into a

three-dimensional structure anchored to multiple surfaces. The progression is driven by two coupled mechanisms:

(i) Shock-Enhanced Wall Mixing: The intensified bow and reflected shocks at high J compress and heat the sidewall boundary layers, creating localized ignition-favorable environments.

(ii) Vortical Redistribution: The strengthened and restructured HSV system actively distributes combustion intermediates, linking the central reaction zone to peripheral stabilization points on the sidewalls and feeding the large-scale CVP.

This spanwise perspective confirms that flame stabilization in a confined supersonic transverse jet is not a singular process but a networked phenomenon, orchestrated by the interplay of compressible shocks and organized vortical transport. The higher maximum OH concentration in the lateral (near-wall) plane quantitatively supports the observation of flame enhancement and "corner trapping" along the lower wall. The wall provides a stable, high-pressure environment where mixing from the HSV can sustain vigorous combustion, even as the free-stream vortex cores remain extinguished.

Local extinction is governed quantitatively by a dual threshold of strain rate and pressure. In the near-wall region, flames survive only where strain remains below $|S| \approx 5.2 \times 10^6 s^{-1}$ and pressure exceeds ≈ 2.5 bar. Vortex cores-regions of extreme strain—consistently exhibit elevated HO_2 (a chain-termination marker) and correspond to flame voids, confirming that high scalar dissipation disrupts the radical pool.

The systematic comparison of flame structure across momentum-flux ratios reveals a clear progression in near-wall combustion completeness. At the lowest J, OH concentrations remain consistently high ($Y_{OH} > 0.008$), indicating robust, continuous combustion (Fig. 22d). At J=3.0, localized mixture-limited suppression emerges, producing condensed pockets of very low OH ($Y_{OH} \approx 0 - 0.002$) where over-rich mixtures cannot ignite, alongside regions of complete reaction loss (Fig. 22e). At the highest momentum flux ratio (J=5.87), OH fields become continuously distributed across a wide range of values ($0 < Y_{OH} < 0.036$), reflecting a highly intermittent combustion regime where vigorous vortical structures simultaneously create fuel-rich pockets that remain non-flammable and elevate strain enough to cause local extinction in the remaining flammable zones (Fig. 22f). Thus, increasing J shifts the dominant limitation from strain-induced extinction toward mixture-driven suppression, fragmenting the flame zone despite stronger jet penetration and more developed vortical systems.

This work provides a resolution to the historical discrepancy regarding flame quenching by identifying strain-driven scalar dissipation as the primary cause for flammable mixture, irrespective of how the susceptible flow region is generated.

(i) In Gamba's experiments, quenching was spatially correlated with an inlet-ramp-generated expansion fan—a geometric feature specific to their setup.

(ii) In the present confined channel (which lacks an inlet ramp), quenching occurs in inherent expansion regions that emerge downstream of the shock train (Section 4.1).

Critically, both configurations exhibit intense vortical structures (CVP, KH rollers) within these expansion zones, producing locally extreme strain rates. The present data show that flame extinction is consistently linked to strain levels that exceed chemical time scales ($Da < 1$), accompanied by elevated HO_2 concentrations—a marker of chain-termination chemistry.

Thus, expansion regions—whether generated by an inlet ramp or by the confined jet-crossflow interaction—are markers of susceptibility, not the direct cause of quenching. The sufficient condition is vortex-amplified strain, which elevates scalar dissipation and disrupts the radical pool. This decoupling of correlation (expansion) from causation (strain) unifies the observations of Gamba et al. and Zhao et al. into a general principle: large-scale flow features define where quenching is likely, but fine-scale vortical strain executes it. This

is evidenced in Fig. 12a, where re-ignition occurs within the effective expansion region ($x \approx 20 - 25$ cm, Fig. 2a) once the local strain rate decays sufficiently—demonstrating that quenching depends on strain.

The findings underscore that confinement, momentum flux ratio, and inlet geometry collectively set the balance between shock- and vortex-dominated combustion. In confined configurations, sidewall shock impingement and horseshoe vortex lifting enable three-dimensional flame anchoring absent in unconfined flows. Design strategies for stable, efficient supersonic combustion must therefore account for both global shock-vortex stability and local strain-limited quenching, ensuring that flame-holding zones reside in sheltered, high-pressure, low-strain regions—often near walls or within vortex braids—while avoiding vortex cores and intense shear-layer rollers. The present conclusions are drawn from a single confined geometry with a hydrogen-air system. Generalization to other configurations (e.g., hydrocarbon fuels) should be validated in future work

Acknowledgements. The author is grateful to Dr. Alexei Poludnenko for providing the Athena-RFX++ code, which was essential for this work. Computational resources were provided by the University of Connecticut. The author is thankful for the valuable discussions with Calvin Colby. Finally, the author extends gratitude to the anonymous reviewers for their time and valuable feedback, which significantly improved the quality of this manuscript.

Funding. This research was supported by the Office of Naval Research under Award No. N00014-23-1-2461 (Program Manager: Dr. Eric Marineau).

Declaration of interests. The authors report no conflict of interest.

Data availability statement. The data that support the findings of this study are openly available upon request.

Author ORCIDs. A. Essa, https://orcid.org/0000-0002-7334-1127

REFERENCES

Attili, Antonio, Bisetti, Fabrizio, Mueller, Michael E & Pitsch, Heinz 2014 Formation, growth, and transport of soot in a three-dimensional turbulent non-premixed jet flame. *Combustion and flame* **161** (7), 1849–1865.

Ben-Yakar, A & Hanson, RK 1998 Experimental investigation of flame-holding capability of hydrogen transverse jet in supersonic cross-flow. In *Symposium (International) on combustion*, , vol. 27, pp. 2173–2180. Elsevier.

Candler, Graham V, Cymbalist, Niccolo & Dimotakis, Paul E 2017 Wall-modeled large-eddy simulation of autoignition-dominated supersonic combustion. *Aiaa Journal* **55** (7), 2410–2423.

Dickmann, Dean A & Lu, Frank K 2009 Shock/boundary-layer interaction effects on transverse jets in crossflow over a flat plate. *Journal of Spacecraft and Rockets* **46** (6), 1132–1141.

Essa, Ahmed 2026 The emergence of a shock-driven global mode in a confined supersonic channel: Beyond rayleigh flow. *Preprint* .

Ezra, Moran & Kozak, Yoram 2023 Development of an immersed boundary method for high-speed compressible flows. In *AIAA SCITECH 2023 Forum*, p. 1401.

Fu, Yaowei, Yu, Changping, Yan, Zheng & Li, Xinliang 2019 Dns analysis of the effects of combustion on turbulence in a supersonic h2/air jet flow. *Aerospace Science and Technology* **93**, 105362.

Gamba, Mirko, Miller, Victor, Mungal, Godfrey & Hanson, Ronald 2012 Combustion characteristics of an inlet/supersonic combustor model. In *50th AIAA aerospace sciences meeting including the new horizons forum and aerospace exposition*, p. 612.

Gamba, Mirko, Miller, Victor, Mungal, M Godfrey & Hanson, Ronald 2011 Ignition and flame structure in a compact inlet/scramjet combustor model. In *17th AIAA International Space Planes and Hypersonic Systems and Technologies Conference*, p. 2366.

Gamba, Mirko & Mungal, M Godfrey 2015 Ignition, flame structure and near-wall burning in transverse hydrogen jets in supersonic crossflow. *Journal of Fluid Mechanics* **780**, 226–273.

Gevorkyan, L, Shoji, T, Getsinger, DR, Smith, OI & Karagozian, AR 2016 Transverse jet mixing characteristics. *Journal of Fluid Mechanics* **790**, 237–274.

Glassman, Irvin, Yetter, Richard A & Glumac, Nick G 2014 *Combustion*. Academic press.

Gruber, MR, Nejad, AS, Chen, TH & Dutton, J Craig 1996 Bow shock/jet interaction in compressible transverse injection flowfields. *AIAA journal* **34** (10), 2191–2193.

Hass, Neal, Smart, Michael & Paull, Allan 2005 Flight data analysis of the hyshot 2. In *AIAA/CIRA 13th international space planes and hypersonics systems and technologies conference*, p. 3354.

Huang, Wei 2016 Transverse jet in supersonic crossflows. *Aerospace Science and Technology* **50**, 183–195.

Huang, Wei & Yan, Li 2013 Progress in research on mixing techniques for transverse injection flow fields in supersonic crossflows. *Journal of Zhejiang University SCIENCE A* **14** (8), 554–564.

Jozefik, Zoltan, Harvazinski, Matthew E, Sankaran, Venkateswaran, Dammati, Sai Sandeep, Poludnenko, Alexei Y, Lu, Tianfeng, Kerstein, Alan R, Xu, Rui & Wang, Hai 2024 Modeling of high-speed, methane–air, turbulent combustion, part i: One-dimensional turbulence modeling with comparison to dns. *Combustion and Flame* **263**, 113379.

Karagozian, Ann R 2010 Transverse jets and their control. *Progress in energy and combustion science* **36** (5), 531–553.

Kelso, Richard Malcolm, Lim, TT & Perry, AE 1996 An experimental study of round jets in cross-flow. *Journal of fluid mechanics* **306**, 111–144.

Laurence, SJ, Karl, Sebastian, Schramm, J Martinez & Hannemann, Klaus 2013 Transient fluid-combustion phenomena in a model scramjet. *Journal of Fluid Mechanics* **722**, 85–120.

Li, Xin, Pan, Yu, Liu, Chaoyang & Zou, Junbo 2024 Investigation of hydrogen/air co-flow jet flame propagation mechanism in supersonic crossflow. *Physics of Fluids* **36** (7).

Liang, Chang-hai, Sun, Ming-bo, Liu, Yuan & Yang, Yi-xin 2018 Shock wave structures in the wake of sonic transverse jet into a supersonic crossflow. *Acta Astronautica* **148**, 12–21.

Liu, Chaoyang, Yu, Jiangfei, Wang, Zhenguo, Sun, Mingbo, Wang, Hongbo & Grosshans, Holger 2019*a* Characteristics of hydrogen jet combustion in a high-enthalpy supersonic crossflow. *Physics of Fluids* **31** (4).

Liu, Yuan, Sun, Ming-bo, Liang, Chang-hai, Cai, Zun & Wang, Ya-nan 2018 Structures of near-wall wakes subjected to a sonic jet in a supersonic crossflow. *Acta Astronautica* **151**, 886–892.

Liu, Yuan, Sun, Ming-bo, Liang, Chang-hai, Yu, Jiang-fei & Li, Guang-xin 2019*b* Flowfield structures of pylon-aided fuel injection into a supersonic crossflow. *Acta Astronautica* **162**, 306–313.

Miller, Warrick A, Medwell, Paul R, Doolan, Con J & Kim, Minkwan 2018 Transient interaction between a reaction control jet and a hypersonic crossflow. *Physics of Fluids* **30** (4).

Muppidi, Suman & Mahesh, Krishnan 2006 Two-dimensional model problem to explain counter-rotating vortex pair formation in a transverse jet. *Physics of Fluids* **18** (8).

Nie, Zhongheng, Gao, Wei, Jiang, Haipeng, Zhao, Fengyu & Lu, Zhengkang 2024 Understanding the mechanisms of flame quenching and flame-wall interactions in microchannel. *Applied Thermal Engineering* **250**, 123529.

Poludnenko, Alexei Y, Chambers, Jessica, Ahmed, Kareem, Gamezo, Vadim N & Taylor, Brian D 2019 A unified mechanism for unconfined deflagration-to-detonation transition in terrestrial chemical systems and type ia supernovae. *Science* **366** (6465), eaau7365.

Poludnenko, Alexei Y, Gardiner, Thomas A & Oran, Elaine S 2011 Spontaneous transition of turbulent flames to detonations in unconfined media. *Physical Review Letters* **107** (5), 054501.

Poludnenko, Alexei Y & Oran, Elaine S 2010 The interaction of high-speed turbulence with flames: Global properties and internal flame structure. *Combustion and Flame* **157** (5), 995–1011.

Potturi, Amarnatha S & Edwards, Jack R 2015 Large-eddy/reynolds-averaged navier–stokes simulation of cavity-stabilized ethylene combustion. *Combustion and Flame* **162** (4), 1176–1192.

Rasheed, Imran & Mishra, Debi Prasad 2023 Numerical study of transverse hydrogen injection in high-speed reacting crossflow. *Physics of Fluids* **35** (6).

Sharma, Shivank, Bielawski, Ral, Rauch, Andreas H & Raman, Venkatramanan 2024*a* High-fidelity computational study of high-speed reacting jets in crossflow. In *AIAA SciTech 2024 Forum*, p. 2596.

Sharma, Shivank, Singh, Jagmohan, Angelilli, Lorenzo & Raman, Venkat 2024*b* Interaction of chemical reactions and turbulence in a jet in supersonic crossflow. *Proceedings of the Combustion Institute* **40** (1-4), 105295.

Smart, Michael K, Hass, Neal E & Paull, Allan 2006 Flight data analysis of the hyshot 2 scramjet flight experiment. *AIAA journal* **44** (10), 2366–2375.

Smith, SH & Mungal, MG 1998 Mixing, structure and scaling of the jet in crossflow. *Journal of fluid mechanics* **357**, 83–122.

Stone, James M, Gardiner, Thomas A, Teuben, Peter, Hawley, John F & Simon, Jacob B 2008 Athena: a new code for astrophysical mhd. *The Astrophysical Journal Supplement Series* **178** (1), 137.

Stone, James M, Mullen, Patrick D, Fielding, Drummond, Grete, Philipp, Guo, Minghao, Kempski, Philipp, Most, Elias R, White, Christopher J & Wong, George N 2024 Athenak: a performance-portable version of the athena++ amr framework. *arXiv preprint arXiv:2409.16053* .

Stone, James M, Tomida, Kengo, White, Christopher J & Felker, Kyle G 2020 The athena++ adaptive mesh refinement framework: Design and magnetohydrodynamic solvers. *The Astrophysical Journal Supplement Series* **249** (1), 4.

Sun, Mingbo & Hu, Zhiwei 2018 Formation of surface trailing counter-rotating vortex pairs downstream of a sonic jet in a supersonic cross-flow. *Journal of Fluid Mechanics* **850**, 551–583.

Toro, Eleuterio F 2013 *Riemann solvers and numerical methods for fluid dynamics: a practical introduction*. Springer Science & Business Media.

Viti, Valerio, Neel, Reece & Schetz, Joseph A 2009 Detailed flow physics of the supersonic jet interaction flow field. *Physics of fluids* **21** (4).

Wang, Dayi, Wang, Ziao, Chang, Juntao, Yue, Lianjie, Wang, Gang & Chen, Hao 2024 Experimental and numerical investigation of three-dimensional shock train topology with differently oriented background waves. *Physical Review E* **109** (2), 025103.

Wang, Ziao, Yao, Kai, Chang, Juntao, Yue, Lianjie, Chen, Hao, Huang, Renzhe & Chao, Youchuang 2025 Experimental investigation of shock-wave–streamwise-vortex interaction. *AIAA Journal* **63** (8), 3079–3106.

Xiao, Yanfeng, Zhang, Huanhao, Chen, Zhihua, Zhang, Hui & Zheng, Chun 2024 Numerical investigation on the transverse jet into a supersonic crossflow with different pressure ratios. *Engineering Applications of Computational Fluid Mechanics* **18** (1), 2354760.

Xiong, Bing, Fan, Xiao-qiang, Wang, Zhen-guo & Tao, Yuan 2018 Analysis and modelling of unsteady shock train motions. *Journal of Fluid Mechanics* **846**, 240–262.

Xiong, Dapeng, Sun, Mingbo, Yu, Jiangfei, Hu, Zhiwei, Yang, Yixin, Wang, Hongbo & Wang, Zhengguo 2022 Effects of confinement and curvature on a jet in a supersonic cross-flow. *Proceedings of the Institution of Mechanical Engineers, Part G: Journal of Aerospace Engineering* **236** (16), 3518–3530.

Zhang, Duo, Cao, Donggang, He, Guoqiang, Liu, Bing & Qin, Fei 2019 Investigation on combustion mode and heat release in a model scramjet engine affected by shocks. *International Journal of Hydrogen Energy* **44** (52), 28330–28341.

Zhao, Majie, Zhou, Taotao, Ye, Taohong, Zhu, Minming & Zhang, Hongda 2017 Large eddy simulation of reacting flow in a hydrogen jet into supersonic cross-flow combustor with an inlet compression ramp. *International Journal of Hydrogen Energy* **42** (26), 16782–16792.

Statement of Significance

This study resolves a longstanding debate on flame quenching mechanisms in supersonic transverse jets by demonstrating that vortex-amplified strain—not expansion fans—is the fundamental cause of local extinction. Through high-fidelity simulations, we reveal how shock-vortex interactions drive the transition to global thermoacoustic instability, showing that the counter-rotating vortex pair (CVP) evolves from a passive mixing structure into an active, piston-like driver of system-scale unsteadiness. The counter-rotating vortex pair (CVP) evolves from a passive mixing structure into an active, piston-like driver of system-scale unsteadiness, with cross-correlation analysis confirming that pressure disturbances originate in the CVP core and propagate to the upper wall with a statistically significant 26 μs lead time ($R = 0.13$, $p < 0.01$).

Furthermore, we demonstrate how flame anchoring transitions from two-dimensional sheets to three-dimensional structures via shock-enhanced wall mixing and vortical redistribution. We reconcile the debate between Gamba & Mungal (2015) and Zhao et al. (2017) by showing that their explanations are complementary: expansion regions create susceptible zones where vorticity-mediated strain dominates quenching. We also identify a constant strain rate threshold across momentum flux ratios (J) that precedes intermittent burning and eventual quenching in this confined setup.

These findings advance the fundamental understanding of compressible reacting flows and provide direct insights for designing stable, efficient supersonic combustors.